HEALTH AND MEDICINE

Shine and darkle the blood vessels: Multiparameter hypersensitive MR angiography for diagnosis of panvascular diseases

Wenyue Li[1], Junwei Cheng[1], Chuang Liu[1], Ni Zhang[2], Hua Lin[2], Fangfei He[1,3], Zhihua Gan[1], Peisen Zhang[1]*, Meng Qin[2]*, Yi Hou[1]*

Magnetic resonance angiography (MRA) is pivotal for diagnosing panvascular diseases. However, single-modality MRA falls short in diagnosing diverse vascular abnormalities. Thus, contrast agents combining T_1 and T_2 effects are sought for multiparameter MRA with clinical promise, yet achieving a balance in T_1 and T_2 contrast enhancement effects remains a scientific challenge. Herein, we developed a hypersensitive multiparameter MRA strategy using dual-modality $NaGdF_4$ nanoparticles. Because of the longer tumbling time (τ_R), $NaGdF_4$ nanoparticles can improve the longitudinal relaxivity (r_1), brightening vessels in T_1-weighted sequences. Simultaneously, the regular arrangement of Gd^{3+} in the crystal induces magnetic anisotropy, creating local static magnetic field heterogeneity and generating negative signals in T_2-weighted sequences. Consequently, the efficacy of $NaGdF_4$-enhanced high-resolution multiparameter MRA has been validated in diagnosing ischemic stroke and Alzheimer's disease in rodent models. In addition, the dual-contrast imaging has been realized on swine with a clinical 3.0-T magnetic resonance imaging scanner, highly emphasizing the clinical translation prospect.

INTRODUCTION

Panvascular diseases refer to a series of systemic disorders of arteries, veins, and capillaries, mainly resulting in the injuries to the brain, heart, kidney, and other important organs, and, what is more, the generalized panvascular diseases include cancers, diabetes, immune diseases, etc. (*1*–*3*). These panvascular diseases urgently threaten the public health, and enormous efforts have been invested to improve the diagnosis of angiopathies for prevention and effective treatment of panvascular diseases. In clinic, the detection of vascular abnormalities mainly depends on various angiography technologies, such as digital subtraction angiography (DSA), computed tomography angiography (CTA), computed tomography perfusion (CTP), etc. (*4*–*6*). CTA and CTP are the commonly applied imaging modalities to explore the anatomical and physiological information on vasculature, while DSA is regarded as the gold standard for the diagnosis of angiopathies (*7*–*9*). However, these imageological examinations require patients to not only be exposed to x-ray radiation but also receive iodinated contrast media, which always carry risk of allergic reactions. What is more, DSA is an invasive intervention approach (*9*–*11*).

Owing to the high spatial and temporal resolutions and unlimited detection depth of tissue, magnetic resonance imaging (MRI) has become a pivotal clinical approach to visualize vascular abnormalities without ionizing radiation and invasive intervention, and various specific sequences have been developed for improving the imaging diagnostic accuracy of magnetic resonance angiography (MRA) (*12*, *13*). In clinical practice, the phase-contrast and time-of-flight (TOF) sequences based on blood flow have been developed to acquire high-resolution angiograms. These sequence scans are non-contrast enhanced and always take long scan time that leads to the respiratory motion artifact. The blood flow–dependent nature restricts the accuracy of MRA, especially for the microvessels with complex anatomical structure or slow blood flow (*14*, *15*). For example, TOF is an MRA sequence that relies on blood flow as the physical basis for generating contrast between stationary tissues and moving spins. When blood flow is perpendicular to the imaging plane, the TOF technique provides maximal signal. However, the vascular systems are very complicated, which are difficult to be clearly imaged solely by the blood flow velocity in a certain direction. Thus, numerous MR contrast agents have been developed to enhance the contrast of imaging.

The paramagnetic gadolinium (Gd) chelates and superparamagnetic iron oxide nanoparticles have been approved as T_1- and T_2-weighted contrast agents in clinical practice, respectively (*16*). The Gd chelate derivants, such as Gd–diethylenetriamine pentaacetic acid (DTPA), can shorten the longitudinal relaxation time of protons and brighten the blood pool and, thus, have been dominantly applied in clinical MRI diagnosis of vasculopathy. However, the small-molecular Gd chelates can extravasate from blood vessels and diffuse into intercellular space very soon, not merely resulting in short circulation times but restricting to attain accurate angiograms (*13*, *17*). In addition, T_1-weighted MRA is not suitable for depicting the anatomical structure of vasculature in encephalocele, especially for the cerebral microvasculature (*18*). Compared to T_1-weighted contrast agents, the superparamagnetic iron oxide nanoparticles produce hypointensive signals. By combining with specific sequences, such as susceptibility-weighted imaging (SWI) sequence, the local contrast of vessels can be enhanced greatly; thus, the iron oxide nanoparticles have been considered to be suitable for diagnosis of vasculopathy, especially for the cerebrovascular diseases (*7*, *19*). However, the hemorrhage and pathologic calcification can also lead to negative MRI signals, namely, the intrinsic limitations of single-modality MRI somewhat restrict their applicability in clinical.

[1]College of Materials Science and Engineering and College of Life Science and Technology, Beijing University of Chemical Technology, Beijing 100029, China. [2]Department of Psychiatry and Center for Preclinical Safety Evaluation of Drugs, West China Hospital of Sichuan University, Chengdu 610041, China. [3]CAS Key Laboratory for Biomedical Effects of Nanomaterials and Nanosafety, National Center for Nanoscience and Technology of China, Beijing 100190, China.
*Corresponding author. Email: houyi@iccas.ac.cn (Y.H.); qinmeng212@scu.edu.cn (M.Q.); zhangps@iccas.ac.cn (P.Z.)

In this context, the contrast agents combining T_1 and T_2 dual modality have been supposed to provide complementary diagnostic information and eliminate the artifacts (*20*–*22*). The ultrasmall iron oxide nanoparticles below 5 nm simultaneously exhibit enhancement in contrast for T_1/T_2 dual-modality MRI because the paramagnetism becomes dominant because of the increased degree of spin disorders on the small particle surface (*23*). Nevertheless, it remains a scientific challenge to balance the T_1 and T_2 contrast enhancement effects, and, briefly, enhancing the T_1 effect by means of reducing the particle size always depresses the T_2 effect of iron oxide nanoparticles. Furthermore, ultrasmall iron oxide nanoparticles can cause signal loss with T_1-weighted MRI at high concentration, limiting its use with T_1-weighted sequences (*24*).

To address these restrictions, herein, we developed a strategy of hypersensitive dual-modality MRA with high resolution based on ultrasmall Gd-doped inorganic nanoparticles $NaGdF_4$ as a multiparametric MRI contrast agent. Considering the T_1 signal enhancement mechanism, the r_1 of nanoparticles stems from their surface Gd^{3+} ions. With appropriate diameters, these ultrasmall nanoparticles exhibit a relatively large specific surface area, and surface Gd^{3+} ions of nanoparticles undergo τ_R compared to small-molecular contrast agents, thus improving the r_1 much more greatly than small-molecular Gd chelates, as illustrated in Fig. 1A. Specifically, the clinical Gd chelates tumble on a picosecond timescale (Gd-DTPA, ~54 ps), while the nanoparticles tumble on a nanosecond timescale; for instance, the τ_R of $NaGdF_4$ nanoparticles is ~453 ns (*25*). Conversely, Gd^{3+} ions within the nanoparticle core do not interact with water protons, but they do contribute to magnetic anisotropy for enhancing the T_2 effect. Specifically, owing to the spin-orbit coupling/magnetic dipole interaction, the Gd^{3+} arranged regularly in the crystal can produce magnetic anisotropy; thus, the paramagnetic $NaGdF_4$ nanoparticles generate magnetic field, leading to the heterogeneity of local static magnetic fields, which reduces T_2-weighted signals, especially, combining with specific sequences, such as SWI. Thus, the contrast agents based on $NaGdF_4$ nanoparticles could brighten and darkle blood vessels in different sequence scanning, respectively (Fig. 1B). Furthermore, the blood circulation time of the nanoparticle-based contrast agents can be improved greatly through biocompatible surface modification with polyethylene glycol (PEG) (Fig. 1C). The ideal magnetic and nano-characteristic properties endow the nanoparticle-based agent to greatly enhance the contrast of MRA than clinical Gd-DTPA agent in a suitable window period. In addition, it is important for clinical application that the aqueous dispersions of $NaGdF_4$ nanoparticles are colorless and clear, so the patients might be more psychologically receptive to the use of these agents rather than the dark injections (the inset in Fig. 1C). A series of animal models of panvascular diseases, including cerebral ischemic stroke and Alzheimer's disease (AD), have been built for imaging studies on a 7.0-T animal MRI scanner with a three-dimensional dynamic contrast enhancement (3D DCE) and SWI sequences, respectively. Furthermore, the translation potential of $NaGdF_4$ nanoparticle–based agents to the clinical settings has been evaluated through MRA of swine on a 3.0-T clinical MRI scanner (Fig. 1D).

RESULTS

Relaxivity measurement and biocompatibility evaluation of $NaGdF_4$ nanoparticles

The performance of the PEGylated $NaGdF_4$ nanoparticles (Fig. 2A) as MRI contrast agents was evaluated on a clinical 1.5-T scanner. As shown in Fig. 2B, according to the linear regression fits of the experimental relaxation rates (R_1 and R_2), the molar longitudinal and transverse relaxivity r_1 and r_2 of the $NaGdF_4$ nanoparticles are 5.04 and 7.98 mM^{-1} s^{-1}, which are 2.3- and 2.6-fold than those of Gd-DTPA (2.24 and 3.08 mM^{-1} s^{-1}), respectively, so it is reasonable to expect that the $NaGdF_4$ nanoparticles can serve as multiparametric MRI contrast agent.

Satisfying colloidal stability in physiological environment is a critical prerequisite for the biomedical applications of $NaGdF_4$ nanoparticles as well since it governs the biodistribution and metabolism of the nanoparticles. Therefore, the colloidal stability of PEGylated $NaGdF_4$ nanoparticles in water and normal saline (NS) was evaluated by dynamic light scattering method. As shown in Fig. 2C, the dispersion of $NaGdF_4$ nanoparticles in water and NS both kept them transparent without aggregation, and the hydrodynamic size of $NaGdF_4$ nanoparticles remained stable (fluctuating from 13.70 to 15.35 nm during the period of 7 days) both in water and NS.

As an intravenously administrated MRI contrast agent, the biosafety features are of great significance. The cytotoxicity of the current nanoparticles was first evaluated using human umbilical vein endothelial cells through cell counting kit-8 assay, and Gd-DTPA served as the control. As illustrated in Fig. 2D, both the $NaGdF_4$ nanoparticles and Gd-DTPA did not exhibit obvious cytotoxicity, and more than 80% of the cells were still viable that even the Gd concentration reached 5 mM, which is much higher than the maximal Gd concentration in blood (~1.33 mM) of nanoparticles in the following in vivo imaging studies (the circulating blood volume of mice is ~72 ml/kg) (*26*). In addition, the hemocompatibility feature of nanoparticles was also assessed. Considering that the red blood cells (RBCs) will be lysed in hypotonic solution, the water was set as the positive control and the isotonic NS were set as the negative controls, which are represented as 100 and 0% hemolysis rate, respectively. On this basis, the hemolysis rate of NS solution of nanoparticles with a series of Gd concentrations was calculated. As displayed in Fig. 2E, at the Gd concentrations ranging from 0.01 to 5 mM, the hemolysis rates of the NS solutions of PEGylated $NaGdF_4$ nanoparticles were lower than 2.0%, which is far from the safety threshold of hemolysis rate (5%) according to the American Society for Testing and Materials guideline (*13*, *27*). In addition, the stability of $NaGdF_4$ nanoparticles under physiological conditions was evaluated. Specifically, $NaGdF_4$ nanoparticles were incubated in both fetal bovine serum (FBS) and 10% FBS solutions to mimic physiological conditions, and any potentially released free Gd^{3+} was collected by using ultrafiltration every 2 days, followed by inductively coupled plasma mass spectrometry analysis over 14 days after incubation. As depicted in fig. S5, there was no increase in Gd^{3+} content in the filtrate over time, indicating the stability of $NaGdF_4$ nanoparticles in FBS without Gd^{3+} release. Overall, these results confirmed the high biosafety features of PEGylated $NaGdF_4$ nanoparticles.

Pharmacokinetics is a critical factor influencing the clinical applicability of MRI contrast agents. As an intravenously administrated MRI nano-agent, the blood half-life of the current $NaGdF_4$ nanoparticles should be determined. As displayed in Fig. 2F, through fitting with a mono-compartment model, the blood half-life of $NaGdF_4$ nanoparticles was extracted to be 294.4 min, which is 19 times longer than that of Gd-DTPA (15.1 min). Apart from the blood half-life, the clearance pathway of the nanoparticles has been also investigated. Radioactive ^{68}Ga was labeled on the nanoparticles through the coordination with phosphate groups in PEG ligands (Fig. 2G). The positron emission tomography (PET) imaging was

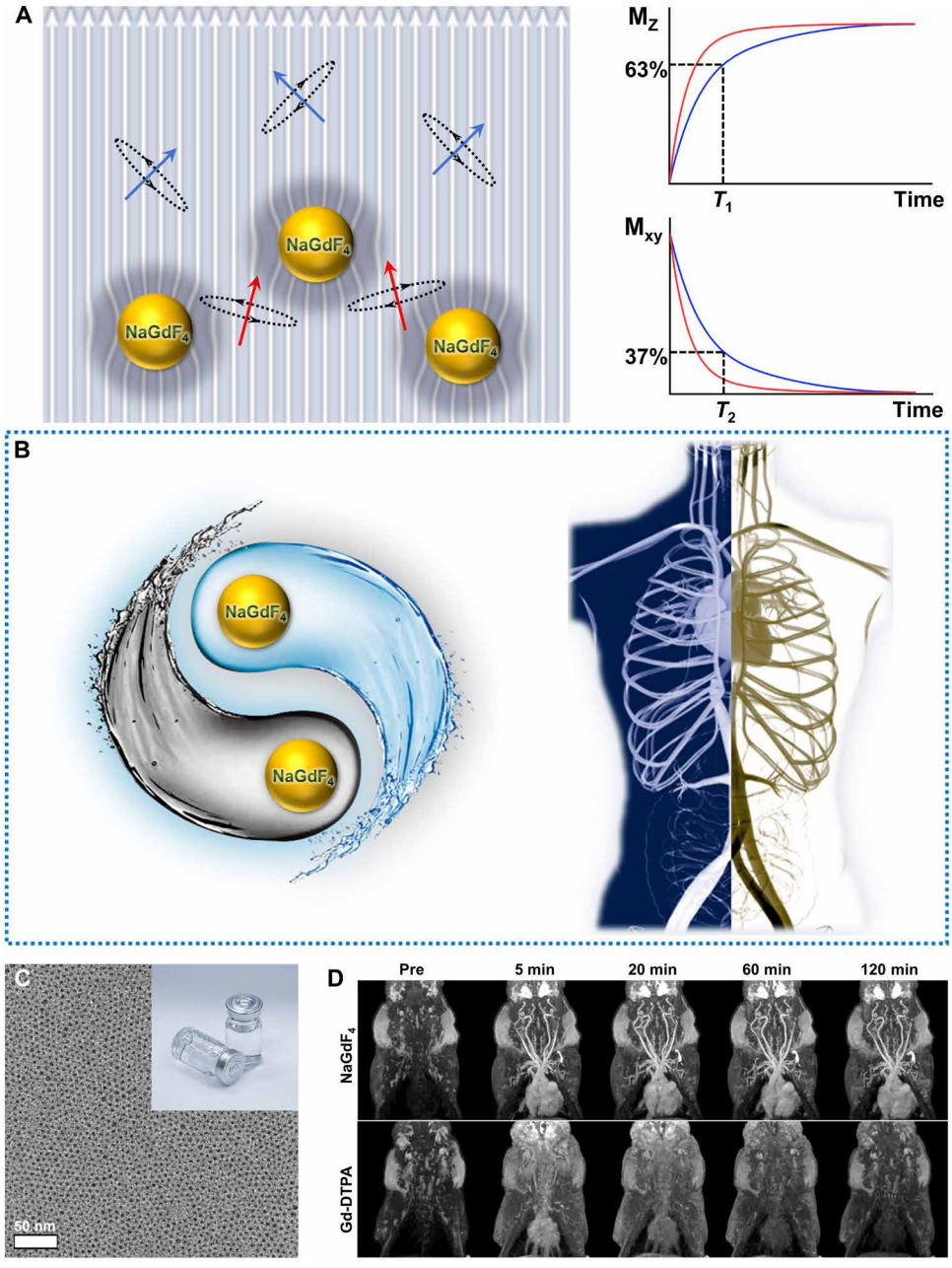

Fig. 1. Illustration of the mechanism diagram and the TEM image and the MR images of $NaGdF_4$. (**A**) The mechanism diagram of ultrasmall Gd-doped inorganic nanoparticles $NaGdF_4$ for hypersensitive dual-modality MRA. (**B**) The schematic diagram of dual shine and darkled blood vessels based on $NaGdF_4$. (**C**) The transmission electron microscopy (TEM) image and the product picture of biocompatible $NaGdF_4$ nanoparticles. (**D**) The MR images of swine with $NaGdF_4$ nanoparticles and Gd-DTPA on a 3.0-T clinical MRI scanner (Note: The $NaGdF_4$ enhanced angiograms shown in 1D are derived from Fig. 6B).

used to display the 3-hour temporal evolution of the biodistribution of PEGylated $NaGdF_4$ nanoparticles in BALB/c mice ($n = 3$). As given in Fig. 2H, from 1 to 3 hours after injection, the radioactive signals in the heart of mice gradually weakened, while the signals in the bladder increased correspondingly. This variation can also be quantitatively characterized through the radioactive intensity analysis shown in Fig. 2I. These results suggested that the current nanoparticles were renally filtered from blood vessels and could be excreted from the body through urinary system.

Multiparameter MRI and MRA with $NaGdF_4$ nanoparticles

Because of the remarkable magnetic and physiological features, the current $NaGdF_4$ nanoparticles are expected to serve as a contrast agent for multiparametric MRA. The in vivo MRI performance of $NaGdF_4$ nanoparticle has been systematically evaluated. Specifically, the multiparametric angiographies and MR imaging, including DCE scanning, T_1-weighted imaging (T_1WI), and SWI scanning, were used to depict the vascular structures of rodent animals.

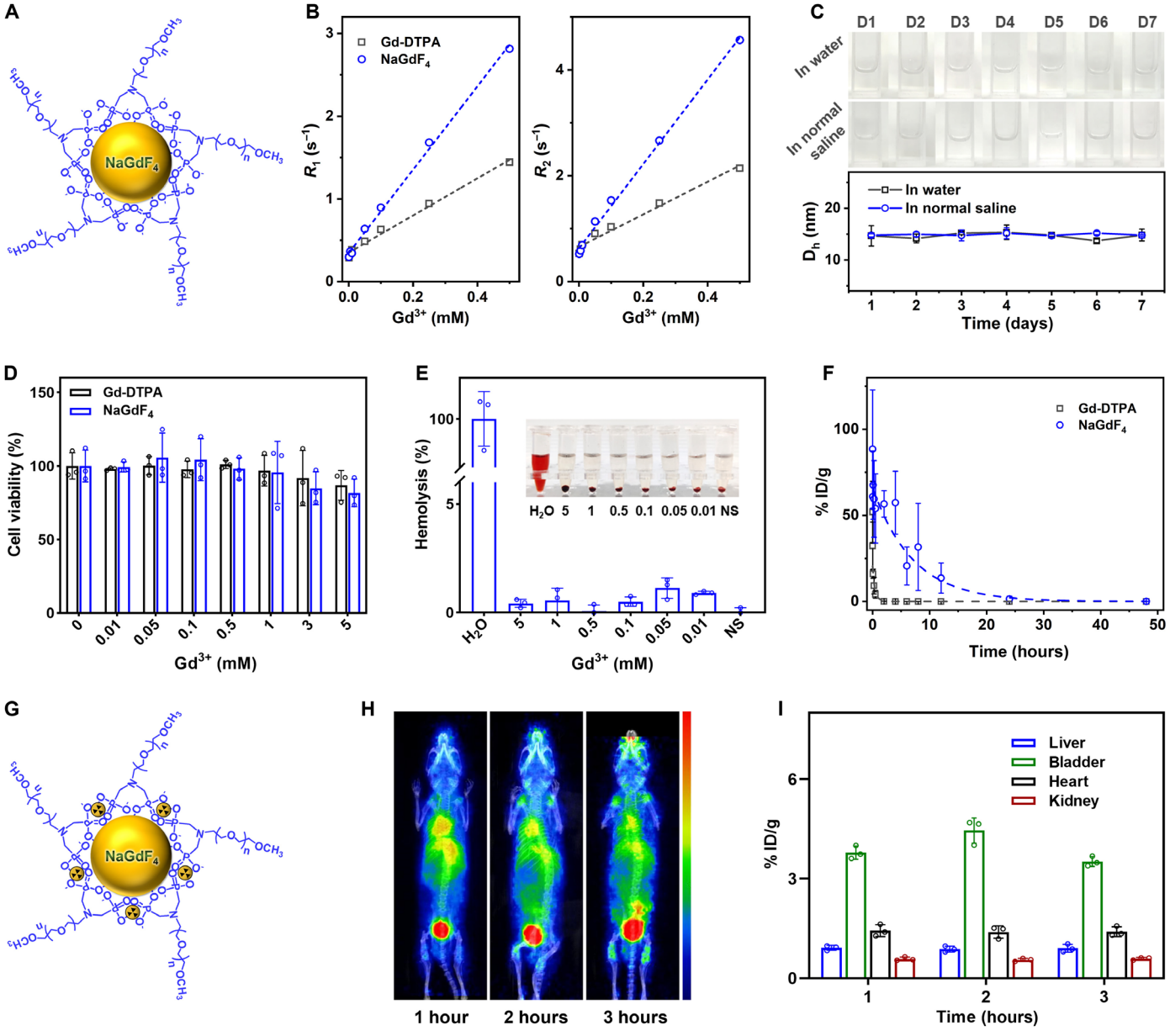

Fig. 2. Characterization of $NaGdF_4$ nanoparticles. (**A**) The schematic diagram of PEGylated $NaGdF_4$ nanoparticles. (**B**) The linear fittings of R_1 and R_2 of $NaGdF_4$ nanoparticles and Gd-DTPA with distinct Gd^{3+} concentration. (**C**) The picture of long-term stability of PEGylated $NaGdF_4$ nanoparticles in water or NS and temporal evolutions of the D_h of PEGylated $NaGdF_4$ nanoparticles in water or NS. (**D**) Viabilities of human umbilical vein endothelial cells after coincubating with $NaGdF_4$ nanoparticles and Gd-DTPA with distinct Gd^{3+} concentration. (**E**) The hemolysis rate analysis of $NaGdF_4$ nanoparticles with different concentrations. Inset, photographs of different solutions containing blood cells after centrifugation. (**F**) Blood clearance profiles of PEGylated $NaGdF_4$ nanoparticles in BALB/c mice ($n = 3$). (**G**) The schematic diagram of PEGylated $NaGdF_4$ nanoparticles labeled ^{68}Ga. (**H**) The PET images of mice acquired at 1, 2, and 3 hours after the intravenous injection of ^{68}Ga-labeled PEGylated $NaGdF_4$ nanoparticles ($n = 3$), together with the time distribution acquired by ^{68}Ga signals in different organs (**I**).

DCE sequence has been widely used in monitoring therapy response and prognosis estimation in patients with vascular dysfunctions and morphological changes (*28*). By using DCE MRI sequence, the angiography performance of $NaGdF_4$ nanoparticles in early phases was firstly evaluated on a 7.0-T animal MRI scanner. The first-pass imaging within 35 s was recorded and was shown in fig. S6. After intravenous injection of $NaGdF_4$ nanoparticles, the strong arterial signals can be observed first, followed by the raised venous signals, realizing the quick vascular imaging to distinguish the arteries and veins of mice. The intravascular signals in $NaGdF_4$-enhanced angiography are mainly dependent on T_1 shortening of the blood rather than flow-related enhancement; therefore, the accurate anatomical structure and morphological change of complicated vascular systems can be better delineated.

As known, increasing the number of excitations (NEX) of a DCE sequence can effectively enhance the image quality but also leads to an extension of scanning time. In clinical practice, because of the short vascular imaging window of small-molecule Gd chelating

contrast agents, the image quality has to be compromised. By contrast, benefiting for the long blood circulating time, the $NaGdF_4$ nanoparticles can provide a longer vascular imaging time window for a DCE sequence with higher spatial resolution but longer scan time. As displayed in Fig. 3 (B and D) and movies S1 and S2, the delayed DCE MR images of mice were obtained at ~10 min after intravenous injection of $NaGdF_4$ nanoparticles. Obviously, with the DCE sequence with higher NEX, the sophisticated whole-body vasculatures of mice, including the main arteries, veins, and even tiny vessels with submillimeter diameter, can be clearly delineated. According to the corresponding atlases of the mice shown in Fig. 3 (A and C), the clinically important vessels, such as the left common carotid artery, precava, left subclavian artery, and aortic arch in the heart; the hepatic artery and right/intermediate/left hepatic vein in the liver; renal artery (RA) and renal vein (RV) in the kidney; and their multigrade branching, can be identified readily, even the

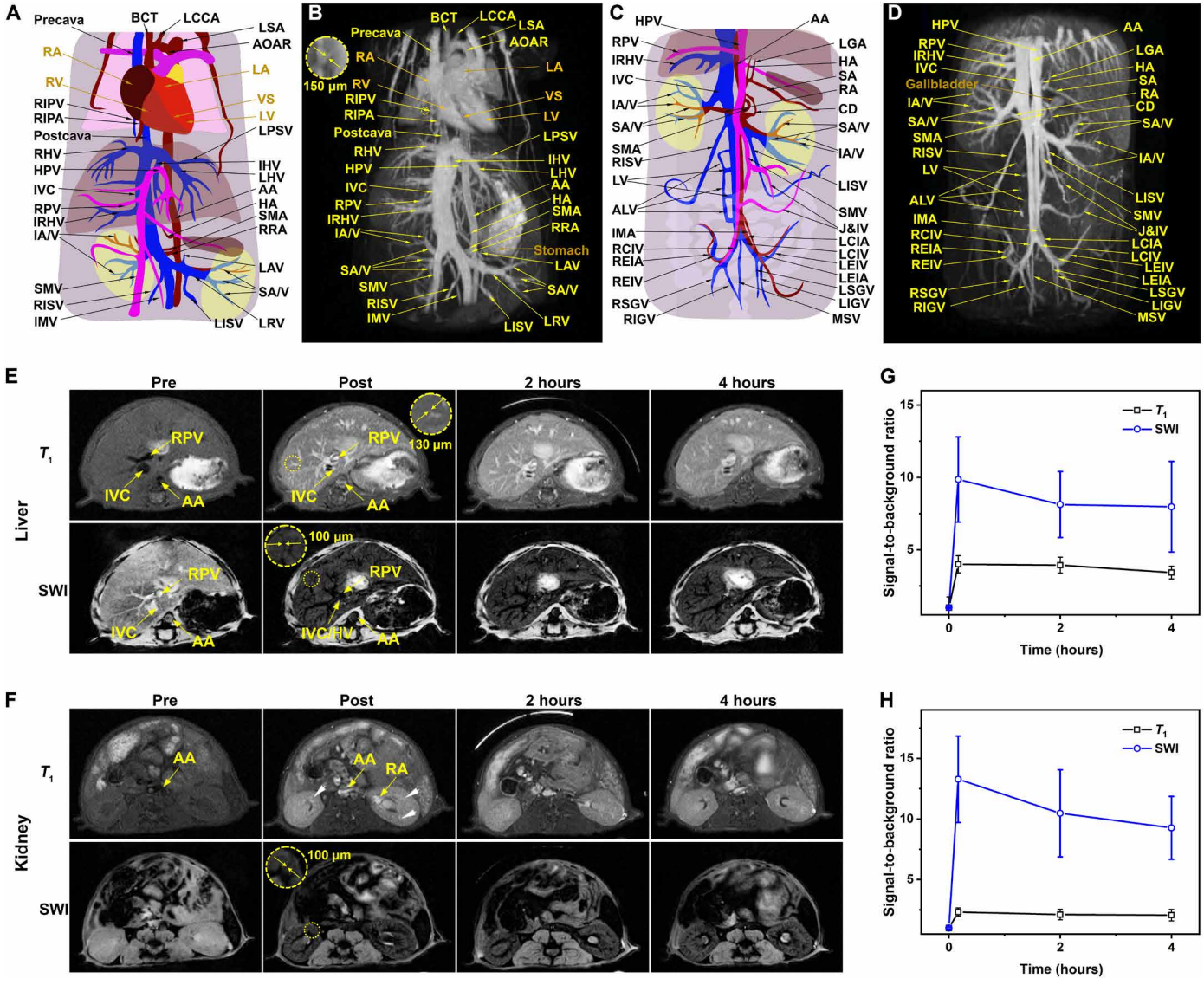

Fig. 3. Chest and abdominal cavity 3D MRA of mice with $NaGdF_4$. The schematic illustration of 3D MRI vascular structures from heart to kidney (**A**) and from kidney to lower limbs (**C**), DCE-MRI of hepatorenal angiography of mice from heart to kidney (**B**), and from kidney to lower limbs (**D**) with PEGylated $NaGdF_4$ nanoparticles after 5 min administration. T_1 MRI and SWI of liver (**E**) and kidney (**F**) of mice with pre-contrast, post-contrast (5 min), after 2 and 4 hours. The temporal evolution of the average intravascular signal intensity ratio of vascular and organs of liver (**G**) and kidney (**H**). Abbreviations: RIPV, right inferior pulmonary vein; RIPA, right inferior pulmonary artery; R/I/LHV, right/ intermediate/left hepatic vein; HPV, hepatic portal vein; IVC, inferior vena cava; RPV, right portal vein; IRHV, inferior right hepatic vein; IA/V, interlobar artery/vein; SMV, superior mesenteric vein; R/LISV, right/left internal spermatic vein; IMV, inferior mesenteric vein; BCT, brachiocephalic trunk; LCCA, left common carotid artery; LSA, left subclavian artery; AOAR, aortic arch; LPSV, left posterior supramarginal vein; AA, abdominal aorta; HA, hepatic artery; SMA, superior mesenteric artery; RRA, right renal artery; LAV, left adrenal vein; SA/V, segmental artery/vein; LRV, left renal vein; LV, lumbar vein; ALV, ascending lumbar vein; IMA, inferior mesenteric artery; R/LCIV, right/left common iliac vein; R/LEIV, right/left external iliac vein; R/LEIA, right/left external iliac artery; R/LSGV, right/left superior gluteal vein; R/LIGV, right/left inferior gluteal vein; LGA, left gastric artery; SA, splenic artery; RA, renal artery; CD, cystic duct; J&IV, jejunal and ileal veins; R/LCIA, right/left common iliac artery; MSV, median sacral. At the heart: L/RA, left/right atrium; L/RV, left/right ventricle; VS, ventricular septum.

slow-flowing tiny vessels as thin as 150 μm in diameter. These vascular identification results highlight the excellent spatiotemporal resolution of $NaGdF_4$-enhanced MRA.

Apart from the DCE MRI that focuses on the passage of a contrast agent within the vasculatures, the contrast-enhanced T_1-weighted MRI can produce the tissue contrast by different T_1 relaxation times. In comparison with the DCE sequence, the T_1-weighted sequence has higher spatial resolution of different tissues, but the scanning time of this sequence is relatively longer. Beneficial from the high r_1 and appropriate blood half-life of the $NaGdF_4$ nanoparticles, the vascular structures are also expected to be visualized through T_1-weighted MRI. As shown in Fig. 3 (E and F), the reticular vascular systems of the liver and kidney can be clearly visualized after the injection of the $NaGdF_4$ nanoparticles. Within the hepatic region, before intravenous injection of the $NaGdF_4$ nanoparticles, only the margin of relatively large vessels in the liver such as the right portal vein (PV), abdominal aorta (AA), inferior vena cava, etc., can be vaguely observed. In contrast, after administration, the microvessels, including the branches of hepatic veins (HVs) and PV, could be clearly delineated by the bright T_1 signals. Specifically, the finest details of the tertiary branches of arteries with the diameter of ~130 μm can be distinguished. With respect to the renal region, only great vessels, such as AA, could be observed in pre-contrast images. However, the different levels of branches of the RA and RV could be visualized with the enhancement of PEGylated $NaGdF_4$ nanoparticles (indicated by the white arrow).

Compared to the DCE and T_1WI sequences, SWI sequence as an essential sequence in the routine MRI strategy for assessing the patients with suspectable cerebrovascular diseases has been used in the current study. Since SWI is highly sensitive to magnetic substances, the current $NaGdF_4$ nanoparticles are expected to improve the visualization of vascular structures. As presented in Fig. 3 (E and F), after $NaGdF_4$ administration, the negative signals of vasculatures quickly appeared in hepatic and renal regions of health mice. In comparison with T_1WI, the smaller branches of HV and PV can be depicted clearly in SWI with a higher resolution. The fourth and even fifth generation of branches of the arteries and veins with the diameters of approximately 100 μm could be distinguished. The 3D DCE, T_1-weighted, and SWI images of mouse liver and kidney were acquired before and after intravenous injection of the clinically used small-molecular contrast agent Gd-DTPA. As shown in fig. S7, vascular signals in these imaging sequences showed minimal improvement, and microvessels in the liver and kidney were less distinguishable following the Gd-DTPA enhancement. These results underscore the superior vascular imaging capabilities of $NaGdF_4$ nanoparticles in multiparameter hypersensitive MRA.

To quantitatively assess the imaging performance of nanoparticle in T_1WI and SWI, the temporal evolution of the average intravascular signal-to-surrounding tissue background ratio in these two sequences was recorded. As given in Fig. 3 (G and H), the absolute value of signal-to-background ratios in $NaGdF_4$-enhanced T_1WI and SWI was obviously alterant. In detail, in terms of the liver, in comparison with the tissue, the intensity of blood vessels enhanced 4.00 times in T_1WI and 9.86 times in SWI, indicating the high signal-to-background ratio in MRI. For the kidney imaging, the enhanced intensity of T_1WI is 2.31 times and the SWI is 13.28 times. In the long run, the vessels could retain an instantly contrast state without apparent attenuation in 4 hours.

Therefore, with the enhancement of the current $NaGdF_4$ nanoparticles, the DCE MRA, T_1WI, and SWI vascular imagings can be acquired with high resolution. These three imaging modalities complement each other and provide comprehensive strategies for diagnosing various clinical indications at different imaging levels. For example, after the enhancement by the nanoparticles, the vascular anatomical structures can be rapidly depicted by DCE imaging, the correlation between vessels and the surrounding tissues can be better reflected in T_1WI images, and the more sophisticated microvessels can be distinguished with SWI. For a specific clinical indication, these MRI modalities can undoubtedly offer a more comprehensive range of physiological and pathological information, thereby maximizing the effectiveness of the diagnostic process.

Diagnosis of CNS diseases

Central nervous system (CNS) diseases, such as the cerebrovascular disease and the neurodegenerative disease, are often associated with a diverse range of vascular abnormalities, including arteriovenous malformations, variations in blood perfusion, and changes in vascular permeability (*29*–*31*). In this context, the $NaGdF_4$ nanoparticle–based MRI strategy developed in this study was used to unravel the vascular lesions of the brain.

To evaluate the feasibility of the $NaGdF_4$ nanoparticle–based MRI strategy in CNS diseases diagnosis, the anatomical structures of cerebral vessels were visualized through different nanoparticle-enhanced MRI sequences. The 3D DCE MRA of the mouse head and neck after contrast enhanced by PEGylated $NaGdF_4$ nanoparticles is shown in Fig. 4A. After intravenous injection, the important cephalic and cervical vessels in clinical practices, such as the basilar artery (BA), vertebral artery (VA), and transverse facial artery, can be clearly identified. Furthermore, the tiny vessels in the brain, such as the superficial superior sagittal sinus (SSS), transverse sinus, and the deeper posterior cerebral artery (PCA), which are closely related to cerebrovascular disease, were also clearly visible [vascular identification of the brain refers to the previous work (*13*)]. Therefore, the PEGylated $NaGdF_4$-enhanced 3D MRA of cephalic vessels can be promisingly served as a rapid and reliable procedure for precise evaluation of brain vascular diseases.

According to the remarkable visualization of smaller vessels, the $NaGdF_4$-enhanced SWI has been used for visualizing the spatial distribution of the microvessels in the mouse brain. As provided in Fig. 4B, the $NaGdF_4$-enhanced SWI is able to image the vasculature in brain parenchyma. After injection of $NaGdF_4$ nanoparticles, the hippocampus, thalamus, and ventricle of the brain can be distinguished more clearly. In addition, cerebral vessels such as SSS, interior sagittal sinus (ISS), and internal cerebral vein (ICV) can be better identified. However, after intravenous injection of Gd-DTPA, the DCE and SWI images of the cephalic and cervical vessels of mice were less distinguishable (fig. S8). Therefore, the $NaGdF_4$-based multiparameter MRA provides valuable insights for diagnosing CNS diseases, such as AD and acute ischemic stroke, providing a critical complementary option to existing diagnostic approaches.

Delineation of insufficient cerebral blood flow in AD

AD is a prevalent CNS disorder characterized by the progressive decline in cognitive function. In general, the diagnosis of AD is based on neuropsychological, imaging, behavioral studies, etc., but the symptom mostly appears in the late period of AD. Biomarkers suggest that the earliest event in AD is a decrease of cerebral blood flow (*31*). Cerebral hypoperfusion or reduced blood flow in the brain leads to the damage of the glial and neuronal cells. Clinically, the

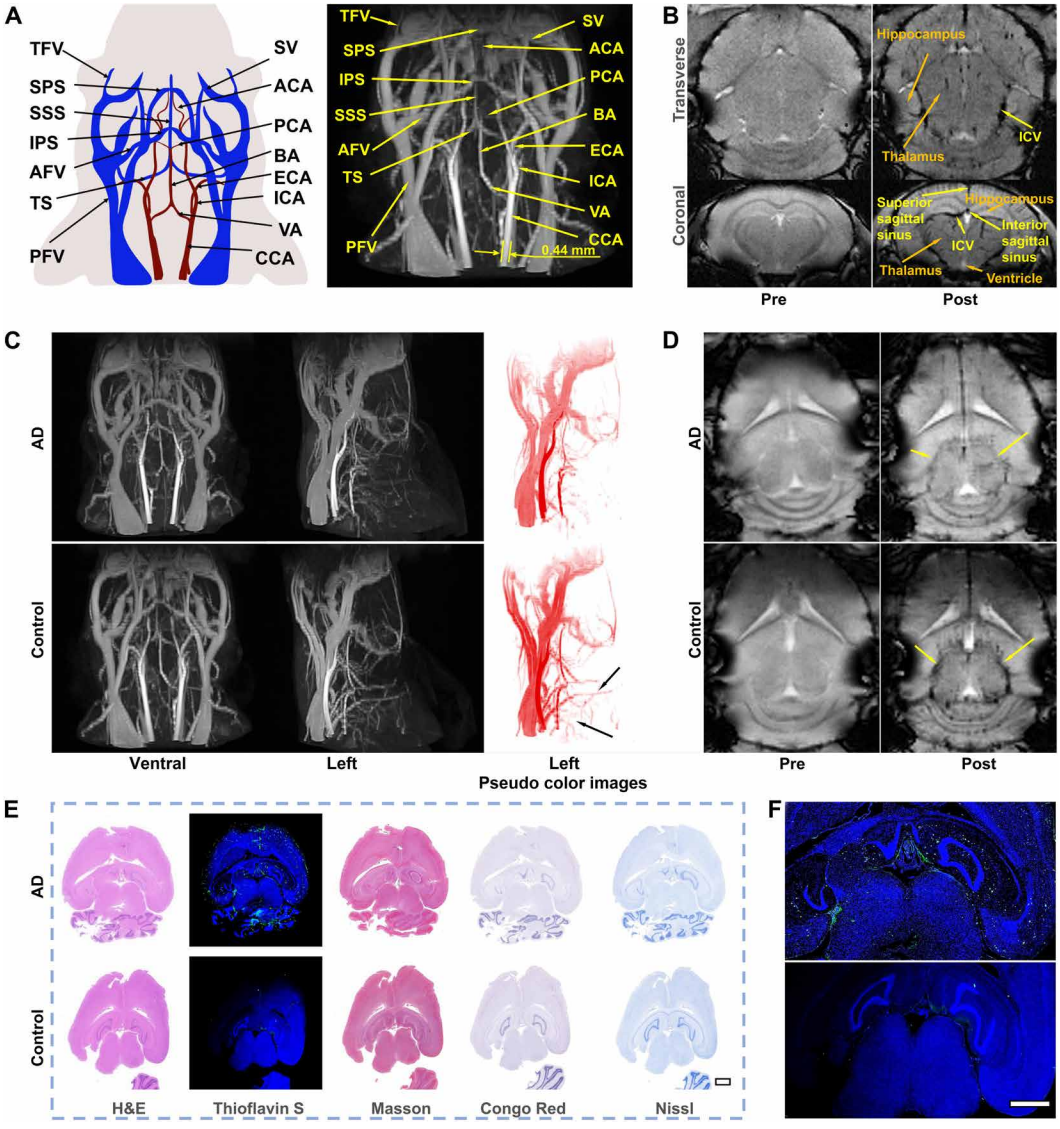

Fig. 4. MRA of AD with NaGdF$_4$. (**A**) Schematic illustration of the vascular anatomic structures of the mouse brain and 3D DCE MRA of the mouse brain enhanced by nanoparticles after 5-min administration. The main blood vessels are identified. (**B**) The transverse position and coronal position of 2D SWI of the mouse brain with pre-contrast and post-contrast (5 min). (**C**) Ventral and left 3D DCE MRA with the pseudo color images of AD and healthy mice brain enhanced by nanoparticles after 5 min administration. (**D**) SWI of AD and healthy mice brain with pre-contrast and post-contrast (5 min). (**E**) H&E, Thioflavin S, Congo red, Masson, and Nissl staining of the brain with AD and healthy mice. The embedded scale bar corresponded to 1 mm. (**F**) The enlarged images of Thioflavin S staining of the brain with AD and healthy mice. The embedded scale bar corresponded to 1 mm. Abbreviations: SV, supraorbital vein; TFV, transverse facial vein; AFV, anterior facial vein; PFV, posterior facial vein; SSS, superior sagittal sinus; TS, transverse sinus; SPS, superior petrosal sinus; IPS, inferior petrosal sinus; ICA, internal carotid artery; ECA, external carotid artery; BA, basilar artery; VA, vertebral artery; CCA, common carotid artery; ACA, anterior cerebral artery; PCA, posterior cerebral artery.

cerebral hypoperfusion in patients with AD is primarily evidenced by reduced cerebral blood flow in the temporoparietal cortex. Specifically, using the medical imaging methods, such as CTP or single-photon emission computed tomography, the status of cerebral blood flow can be mapped through image processing. Nevertheless, these clinically used imaging methods cannot provide continuous cerebral blood flow measurement, and the resolution of these imaging methods is insufficient to accurately pinpoint changes in blood flow within the specific blood vessels (*32*–*34*). In this context, accurate visualization of cerebral vessels with inadequate cerebral perfusion can provide more accurate diagnostic information for early AD.

As shown in Fig. 4C and movies S3 and S4, the DCE angiograms in the ventral and left direction displayed the bright cerebrovascular structures of both AD mouse and healthy mouse after intravenous injection of nanoparticles. There is no difference among the major blood vessels such as BA, internal carotid artery (ICA), common carotid artery (CCA), posterior facial vein, etc. in the ventral direction, but in the left direction, some other microvessels can be observed in the healthy mouse rather than in the AD mouse, especially in the left pseudo color images (black arrows) in Fig. 4C. It may be that decreased blood flow leads to low signal of tiny blood vessels in the AD mouse. SWI sequence was further applied

for visualizing the cerebral microvessels in mice brain, with the aim of reflecting the differences in hypoperfusion between AD and healthy brains. As displayed in Fig. 4D, after the administration of nanoparticles, the vascular signals in SWI of AD and healthy brain are apparent distinct. In particular, all the cerebral vessels in healthy brain exhibited notable black signals in enhanced SW images. However, the corresponding vascular signals in AD brain are much weaker, especially for the vascular signals surrounding the circumferential cistern area of brain (yellow arrow). According to the atlas of the vascular distribution in mice brain, the perfusion surrounding the thalamus and hippocampus, including anterior cerebral artery and PCA, etc., was notably decreased. Therefore, with the enhanced SWI, the hypoperfusion status surrounding the thalamus and hippocampus region in AD brain can be clearly visualized.

To verify the correlation between the MRA and pathological variations of AD brain, the histological analysis was carried out. In Fig. 4E, hematoxylin and eosin (H&E) staining was used to reveal the brain structure of mice, and Thioflavin S, Congo red, Masson, and Nissl stainings were used to show the lesions in the hypoperfusion area. Thioflavin S staining, one staining strategy that can specifically label the mature amyloid-β (Aβ) protein with green fluorescence, was used to confirm the distribution of Aβ in AD brain. As enlarged in Fig. 4F, the green fluorescence signals were predominantly observed surrounding the circumferential cistern and full of the hippocampus region, which were consistent with the brain regions under reduced blood perfusion according to the above SWI result, suggesting that the cerebral hypoperfusion may be associated with the accumulation of Aβ. In addition to Thioflavin S staining, Masson staining was used to mark the collagen (blue), which may be related to the Aβ deposits as well (*35*). In the enlarged images in fig. S9, the presence of blue signals around the hippocampus region indicate the presence of the collagen. The amyloid fibril–binding dye Congo Red can also label the Aβ protein with red color. As shown in fig. S9 (middle), red color can be found near the hippocampus of AD brain, suggesting that the Aβ protein has been accumulated in hippocampus regions, where the brain tissues suffered from the hypoperfusion. Apart from the detection of Aβ protein, the long-term cerebral hypoperfusion may result in glial and neuronal injuries; therefore, Nissl staining was also selected to investigate the neuronal injury. In Nissl staining, the Nissl bodies in several neurons surrounding the circumferential cistern region decreased or disappeared, and the number of neurons in AD is obviously less than that in healthy mouse, indicating the injuries of these nerve cells. Together, through the enhancement of PEGylated $NaGdF_4$ nanoparticles as a dual-modality vascular contrast agent, the hypoperfused vessels surrounding the thalamus and hippocampus were readily identified. This observation aligns effectively with the pathologic regions identified in the brain section, thereby confirming the robustness and reliability of the imaging strategy.

Simultaneous delineation of the arterial occlusion, collaterals, and ischemic penumbra

Acute ischemic stroke and its complications are one of the major leading causes of disability and mortality. The collateral vessels, as a physiologic compensatory response, provide an alternative pathway to preserve the brain tissue from the risk of ischemic injury. Since the collaterals could rescue the ischemic regions, the collateral status determines the region of penumbra, in which the neurons are considered to be salvageable (*7*). In this context, the accurate visualization of the collaterals and the precise delineation of the ischemic penumbra are very crucial for every patient with acute ischemic stroke.

Benefiting from the multimodality MRI performance of the current $NaGdF_4$ nanoparticles, the arterial occlusion, collaterals, and ischemic penumbra after acute stroke are expected to be visualized simultaneously after only one dose of injection through different imaging sequences. As a proof of concept, the right middle cerebral artery occlusion (rMCAO) was mechanically induced in rats to mimic the acute ischemic stroke and the multimodality MRI studies were conducted on a 7.0-T MRI scanner. The clinically commonly used non-contrast–enhanced MRA TOF sequence has been used to display the cephalic and cervical vascular system before administration, as given in Fig. 5A and movie S5. Several big vessels, especially the arteries with fast blood flow velocity, such as VA and BA, could be vaguely observed. In addition, the signals of right external carotid artery and CCA asymmetrically disappeared, indicating the successful establishment of the rMCAO model.

For better visualizing the detailed cerebral vessels through different MRI modalities, the current nanoparticles were used as contrast agent. As indicated in DCE angiography in Fig. 5B and movies S6 and S7, compared with the image before contrast enhancement, the anatomical morphology structure of vasculatures of stroke rat, especially the venous structures, was effectively depicted after injection of nanoparticles. According to the angiogram, the block of right carotid artery did not notably affect the blood flow of the main veins of rat head and neck region. This may be attributed to the post-stroke establishment of collateral circulation including the circle of Willis and arterial anastomosis, which provides compensatory blood stream for the ischemic sites, maintaining the physiological function of brain tissue in pathological state.

In addition to the DCE sequence, the cerebral vessels were further visualized with nanoparticle-enhanced SWI sequences. In comparison with the DCE imaging, the microvessels inside the brain are expected to be depicted with higher resolution. As known, owing to the radial expansion and anastomosis of the arterial artwork (*36*, *37*), the newly formed collaterals can be identified as the asymmetrically hypointense vessels of ischemic side of the brain on SWI. For verifying this hypothesis, the in vivo SW images were acquired before and after intravenous injection of $NaGdF_4$ nanoparticles, as shown in Fig. 5 (C and D). Before contrast enhancement, the leptomeningeal vessels in ischemic cerebral hemisphere were faintly visible, which can be attributed to the increased level of paramagnetic deoxyhemoglobin that can be regarded as endogenous SWI contrast agent. In contrast, in the $NaGdF_4$ nanoparticle–enhanced SWI, the contrast of all the cerebral vessels is strongly enhanced. The tiny cerebral vessels, such as the multilevel branches of SSS, ISS, and ICV, exhibited negative contrast compared with the bright brain tissues. In the enlarged image as shown in Fig. 5E, the tiny vessels in cerebral cortex even as thin as 60 μm in diameter could be distinguished. More vascular signals were observed to be asymmetrically distributed only within the stroke hemisphere. These extraordinary signals displayed a typical macroscopical pattern of vessels, which implied their association with collateral circulation. Therefore, it is reasonable to believe that compared with the contralateral hemisphere, the excess vascular signals distributed surrounding the infarction region should be attributed to the newly formed collateral systems after stroke.

To further understand the collateral vessel signals displayed on the brain SWI of stroke rat, diffusion-weighted imaging (DWI), a type of MRI sequence that has been regarded as the "gold standard"

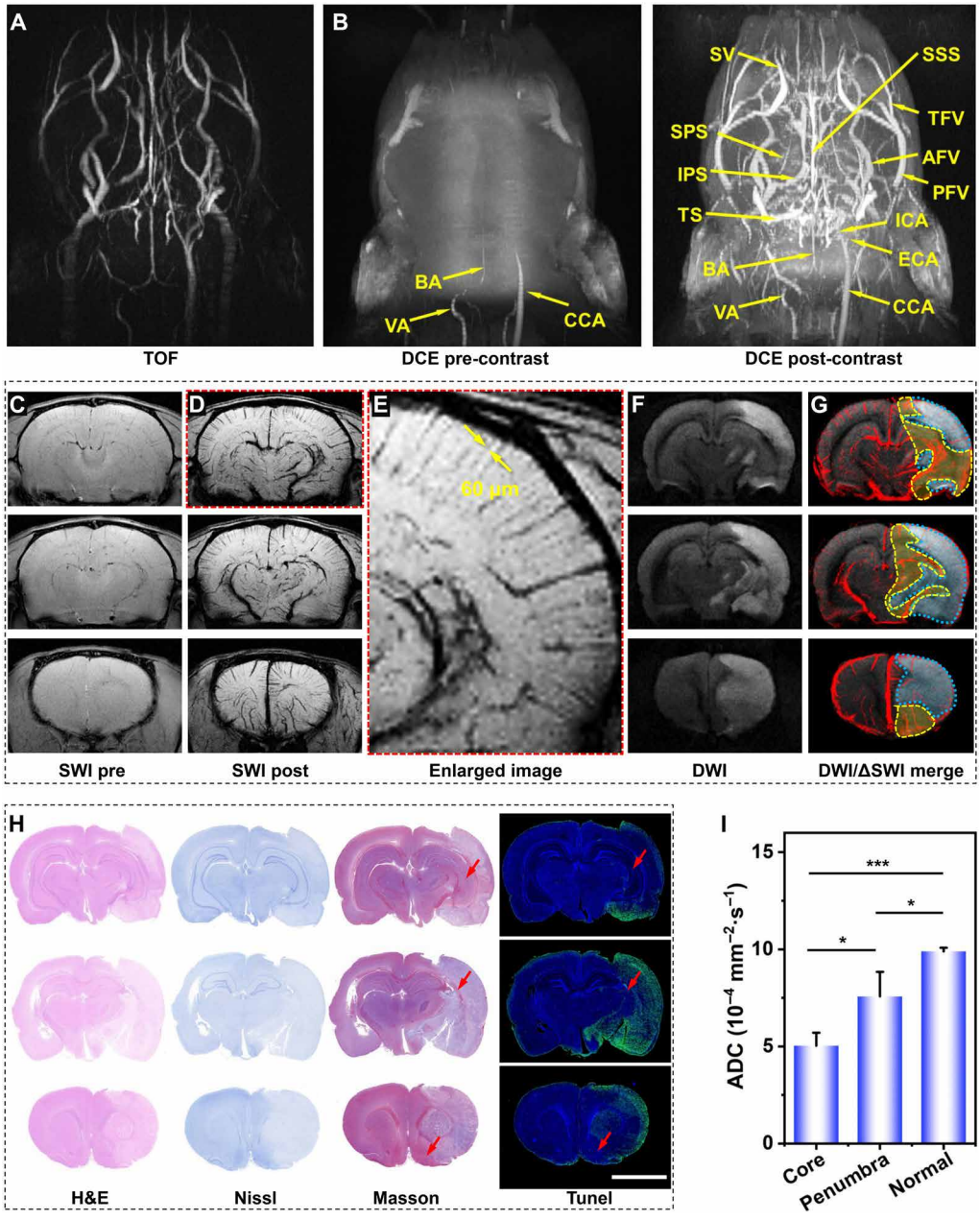

Fig. 5. MRA of stroke with $NaGdF_4$. TOF angiography (**A**) and 3D DCE MRA of the stroke rat enhanced by PEGylated $NaGdF_4$ nanoparticles with pre-contrast and post-contrast (5 min). (**B**). Three representative imaging planes of SWI pre- (**C**) and post 5 min- (**D**) injection of PEGylated $NaGdF_4$ nanoparticles. (**E**) The enlarged image of the upper SW image in (D). Three representative imaging planes of DWI (**F**) and superimposed images of DWI with corresponding ΔSWI (**G**). (**H**) Three representative imaging planes of slice staining analysis with H&E, Nissl, TUNEL, and Masson staining. (**I**) The average ADC values of infarct core identified by the DWI, ischemic region identified by nanoprobe-based ΔSWI, and normal region of contralateral hemisphere in the three imaging planes. Data are shown as means ± SD ($n = 3$). Statistical significance was determined by one-way analysis of variance (ANOVA) with a Tukey's post hoc test (*$P < 0.05$, ***$P < 0.001$). The embedded scale bar corresponded to 5 mm.

for the delineation of the irreversible ischemic core in the clinical practices, was adopted for combined diagnosis of rat stroke. As shown in the Fig. 5F, the range of irreversible infarction was identified in DWI, which is located in the ipsilesional hemisphere with hyperintense signals. Therefore, through combining DWI sequence, the spatial correlation between infarct core and collaterals can be displayed. As shown in Fig. 5G, the SWI image was merged on the corresponding DWI images. The increased vessel clumps were mainly concentrated in the ischemic side and many excess vessels distributed surrounding the infarction core (the blue dotted circle), which is consistent with the general cognition that collateral circulation is generated in the periphery of ischemic core after stroke (*19*). Considering the relationship of the collaterals and the ischemic penumbra, the range of penumbra can be identified as the area of higher collateral density located at the periphery of the infarct core, as indicated by the yellow dotted circle in Fig. 5G.

For further validating the reliability of the identification ischemic penumbra, the water apparent diffusion coefficient (ADC) mapping images were derived from DWI. According to the above identification results of the range of infarct core, ischemic penumbra, and normal brain, the average ADC values of these three regions were recorded, respectively. As shown in Fig. 5I, the average ADC value in infarct core was significantly lower than that of normal region ($P < 0.001$). By contrast, the average ADC value of the penumbra regions identified by the SWI was higher than that of infarct core ($P < 0.05$) but lower than that of normal brain tissues ($P < 0.05$), which is highly consistent with the expectation, i.e., the water diffusion will be maximally restricted in the infarct core, while it will also be impeded to some extent in the penumbra regions. This quantitative result strongly confirms the reliability of the current nanoparticle-based MRI strategy for the simultaneous identification of cerebral infarction and ischemic penumbra.

To further verify the imaging results, the rat was euthanized after imaging. The brain tissues were then extracted and cut into slices of 3 μm for histochemical analysis. In the H&E staining, the extent of ischemic regions can be clearly distinguished through the morphological alterations of cells and tissues, in which the ischemic areas will exhibit a lighter staining color due to the destruction of tissue structure (*38*). As shown in Fig. 5H, the ischemic region shown in H&E staining matched well with infarct core identified in DWI, while most of the brain cells still alive in the penumbra region identified in SWI were located between the normal and ischemic tissues. In addition to H&E staining, Nissl staining was also used to display the morphologies and injuries of nerve cells in the ischemic brain, which can evaluate the overall morphology of the brain. In the diagnosis of stroke, Nissl staining can be applied to designate the infarct core (*39*). As shown in Fig. 5H, the nerve cells in infarct core regions identified by nanoprobe-based MRI strategy exhibited a lighter color compared with normal brain region. This is because the Nissl bodies surrounding the nuclei of nerve cells in the normal brain regions were stained with cresyl violet and presented dark blue granules, while the Nissl bodies were lightly stained or even dissolved in the infarct core regions, suggesting that the nerve cells located in the infarct core were damaged. Apart from Nissl staining, Masson staining was also used to reflect the brain damage. Owing to the large molecular size of aniline blue, the damaged brain tissues with high permeability would be stained in blue color. As indicated in the third column of Fig. 5H, the shape and distribution of abnormal blue regions in the brain slices are highly consistent with the infarct core regions identified in DWI, while the junction where blue merges with purple in slices (as indicated by the red arrow) corresponds to the location of ischemic penumbra in $NaGdF_4$-based MRI. In addition, the result of terminal deoxynucleotidyl transferase–mediated deoxyuridine triphosphate nick end labeling (TUNEL) staining showed the similar results, i.e., the TUNEL-positive cells were predominantly found in the infarct core region but were rare in ischemic penumbra (as indicated by the red arrow), suggesting that the presence of collateral vessels effectively mitigates the damage to nerve cells caused by long-term stroke. These histological results strongly confirmed the reliability of the above imaging strategy for the accurate identification infarct core, collaterals, and ischemic penumbra. Overall, through the $NaGdF_4$ nanoparticle–based MRI strategy, the arterial occlusion, collateral formation, and ischemic penumbra can be precisely visualized after the onset of acute stroke, which can provide more useful information during the management of stroke disease compared with conventional imaging strategy.

Multiparameter hypersensitive MRI with $NaGdF_4$ nanoparticles in large mammal animal

To further assess the potential of $NaGdF_4$ nanoparticles for clinical translation, MRI studies were conducted on large mammals, bama swine, using a 3.0-T clinical human MRI scanner. In this study, the temporal evolution of enhanced 3D time-resolved imaging of contrast kinetics (3D-TRICKS) of swine before and after injection of $NaGdF_4$, over a period of ~120 s, was conducted. As shown in fig. S10, after intravenous injection, $NaGdF_4$ nanoparticles sequentially flow back to the right atrium, pass through the right ventricle, and return to the left atrium and ventricle after completing the pulmonary circulation. Subsequently, they traveled through the aorta to illuminate various arteries at different levels in the entire body, including arteria coronaria, carotid arteries and the branches, subclavian arteries, and AA (Fig. 6A). After the arterial phase (~20 to 30 s after injection), $NaGdF_4$ nanoparticles subsequently enter the different levels of veins. Owing to the appropriate hydrodynamic diameter, the nanoparticles remained within the vessels without extravasation. As a result, both the tiny arteries and veins can be clearly observed during this phase. Therefore, the morphology of the whole blood circulation systems, including the structures of atrium, ventricles and valves; the main arteries originated from the heart; the main veins returned to the heart; as well as the different vascular branches in swine body, can be clearly distinguished and identified (*13*). Overall, the short acquisition time of TRICKS images and higher r_1 of $NaGdF_4$ nanoparticles enable the acquisition of arterial angiograms with great clarity. In addition, the extended angiography window provided by $NaGdF_4$ nanoparticles ensures the successful visualization of venous systems in the subsequent imaging. To obtain the angiograms with higher resolution and take advantage of the long imaging time window offered by the $NaGdF_4$ nanoparticles, the clinical imaging sequences with longer scan times but improved image quality were adopted for the delayed phases of MRA. As given in Fig. 6B (top), the 3D TRICKS sequence, with a higher NEX, was used for angiography. The corresponding angiograms were obtained before injection, as well as at 5, 20, 40, 60, 90, and 120 min after injection. As a result, the cardiovascular structures of swine in each angiogram exhibited high spatial resolution, in which the different microvessels can be clearly distinguished. The strong vascular contrast can be maintained for at least 120 min without notable attenuation until the imaging study is concluded, which highlighted the long imaging window of the current $NaGdF_4$ nanoparticles.

In addition to the TRICKS, the 3D brain volume imaging (3D-BRAVO), a kind of T_1-weighted MRI that are commonly used for the diagnosis of human cerebral diseases, was also adopt for showing the anatomy of swine vessels and tissues. As presented in Fig. 6B (bottom) and movie S8 (the video of the anatomy of swine vessels and tissues after intravenous injection of Gd-DTPA was given in movie S9.), the BRAVO sequence demonstrated even higher imaging resolution compared to the TRICKS MRA sequences, which allowed for a clearer distinguishment of tiny vessels, although the scan time of BRAVO sequences is much longer, typically lasting ~3 to 4 min.

Overall, $NaGdF_4$ nanoparticles displayed their ability to clearly depict the vascular structures both in the early phase with TRICKS

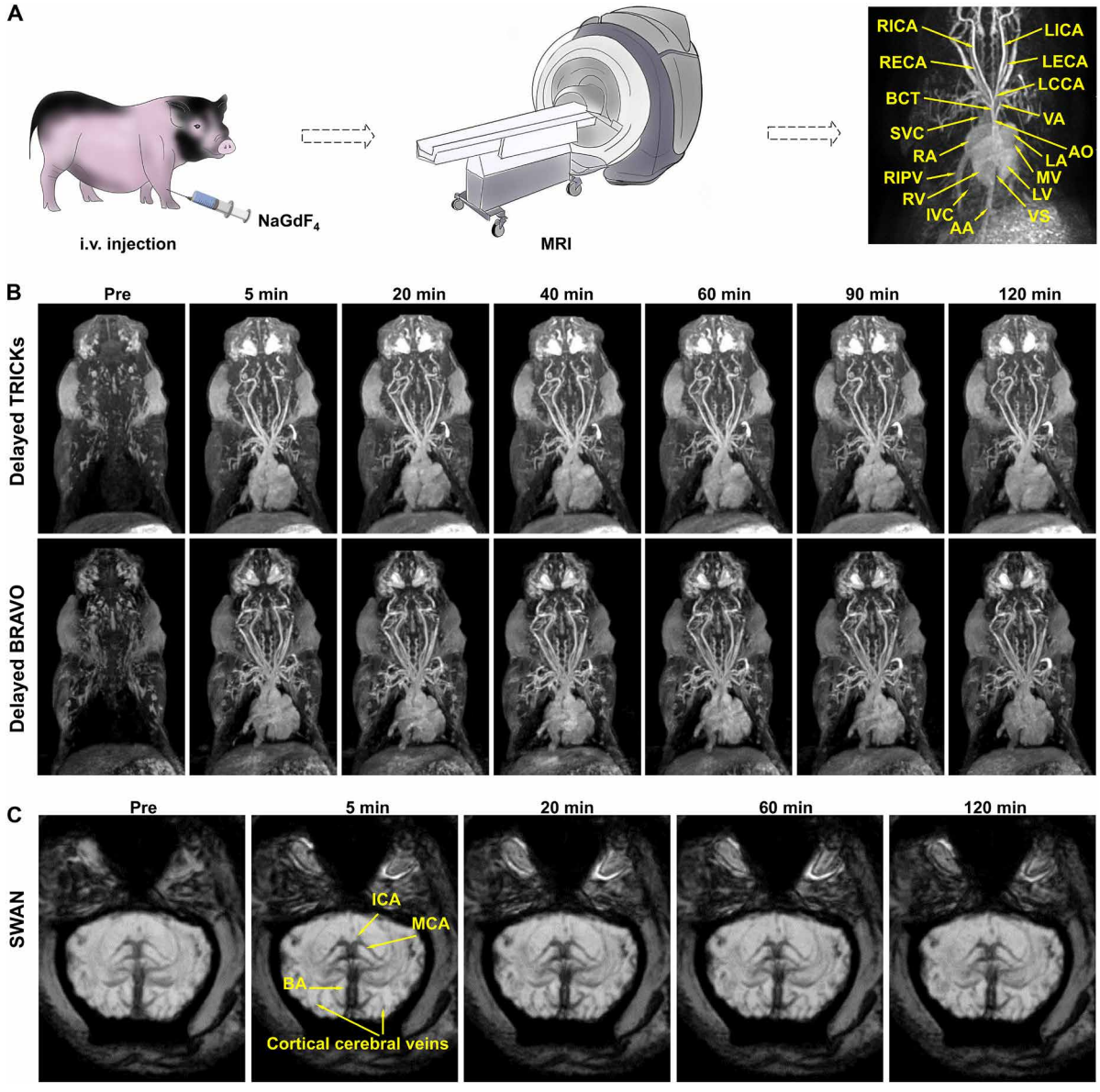

Fig. 6. MRA of swine with $NaGdF_4$. (**A**) Schematic illustration of the procedure of MRA and the vascular identification of swine. (**B**) The 3D TRICKS angiography (top) and 3D BRAVO images (bottom) after $NaGdF_4$ nanoparticles administration. (**C**) SWAN images of brain vessels of swine. Abbreviations: AO, aorta; BCT, brachiocephalic trunk; L/RECA, left/right external carotid artery; L/RICA, left/ right internal carotid artery; LCCA, left common carotid artery; VA, vertebral artery; SVC, superior vena cava; RIPV, right inferior pulmonary vein; IVC, inferior vena cava; AA, abdominal aorta; L/RA, left/right atrium; L/RV, left/right ventricle; VS, ventricular septum; MV, mitral valve; BA, basilar artery; ICA, internal carotid artery; MCA, middle cerebral artery.

sequence and the delayed phases with both TRICKS and BRAVO sequences. In particular, the BRAVO sequence provides higher resolution and facilitates the identification of more microvessels in the $NaGdF_4$ enhanced images. These results underscore the limitation of clinically used low-molecular weight Gd-chelate contrast agents as they necessitate the rapid image acquisition during the initial passage of contrast agents through the target vessels. In contrast, with the prolonged retention of $NaGdF_4$ nanoparticles in bloodstream, high-resolution angiography can be achieved using long scan-time sequences, such as BRAVO. This advancement has the potential to improve the accuracy of diagnosing microvascular diseases, particularly for those involving the micro-venous systems.

Apart from the TRICKS and BRAVO imaging, the transverse plane of cerebral T_2-star weighted angiography (SWAN) was acquired to depict the cerebral arterioles and venules of swine. As shown in Fig. 6C, before the injection of $NaGdF_4$ nanoparticles, several large vessels of brain including BA, ICA, and MCA, can be already observed owing to the deoxyhemoglobin in the bloodstream. In comparison, following the enhancement of nanoparticles, the micro-branches of the vessels in pre-contrast image, as well as more microvessels in the brain cortex, were clearly discernable. As time passes by, the enhanced negative signals are still retained with the long-time retention of $NaGdF_4$ nanoparticles in the bloodstream, highlighting the long imaging window of the nanoparticles. The

swine was fully anesthetized throughout the MRI experiments, leading to similar images at different time points, but slight differences in details can still be observed. This result indicated that the nanoparticles used in this study can enhance the image resolution of SWAN, allowing for an improved cerebrovascular imaging in swine. This SWAN enhancement can be achieved even with a clinical MRI scanner operating at a relatively lower magnetic field strength of 3.0 T, highlighting the clinical potential of the nanoparticles.

The above results indicated that $NaGdF_4$ nanoparticles exhibit outstanding MRA performance in large animals. Through different MRI sequences, the vascular structures of different tissues can be displayed with high resolution, catering to the requirements of diverse clinical indications. Therefore, it can be reasonably speculated that $NaGdF_4$ nanoparticles have the potential to diagnose multiple vascular diseases in larger animals and even in humans. Overall, $NaGdF_4$ exhibits promising clinical translation prospects in the field of vascular disease diagnosis, offering more clinically helpful information.

Biosafety assessment of $NaGdF_4$ on rodent animals

Biosafety concerns often arise when considering the clinical translation of imaging nanoparticles. To dispel this concern, the biosafety of PEGylated $NaGdF_4$ nanoparticles was evaluated on rodent animals. The in vivo hematological and tissue effects resulting from the exposure to the $NaGdF_4$ nanoparticles were firstly evaluated on BALB/c mice. Briefly, eight healthy mice were randomly divided into two groups ($n = 4$), and one group of them were intravenously injected with $NaGdF_4$ nanoparticles at a dosage of 0.1 mmol Gd per kg weight. At 14 days after injection, both two groups of mice were euthanized, and the major organs of the mice were extracted and subjected to the histological analysis, while their blood samples were also collected for blood routine and chemical tests. As shown in Fig. 7A, after injection of $NaGdF_4$ nanoparticles, the mice presented negligible fluctuations in body weight, with no significant difference in comparison with the healthy mice ($n = 4$). According to the blood test results (Fig. 7, B to H), in comparison with the healthy mice, there was no sharp increase or decrease in any serum biochemical parameter at 14 days after injection, and all the parameters remained in the normal range after 14 days. In addition, there was no obvious hepatic or renal toxicity, as evidenced by normal levels of liver function markers [alanine aminotransferase (ALT), aspartate aminotransferase (AST), and gamma-glutamyltransferase (γ-GT)] and kidney function markers [carbamide (UREA), creatinine (CREA), and uric acid, (UA)]. Furthermore, $NaGdF_4$ nanoparticles did not induce inflammation-related diseases or acute hemolysis, as shown by stable levels of white blood cell (WBC), lymphocytes (Lymph#), RBC, platelets (PLTs), mean platelet volume (MPV), and plateletcrit (PCT). In addition to the blood test, H&E staining of the organ slices (Fig. 7I) revealed no abnormal signals in pathological histology or cellular structure, suggesting that $NaGdF_4$ nanoparticles did not induce any inflammation or damage to major organs. In addition, Chlorophosphonazo III (CPN III) rare-earth staining of the organ slices was also carried out, as shown in fig. S11, and no blue or cyan color can be observed in the slices of these organs after 14 days after injection, suggesting that most $NaGdF_4$ have been eliminated from the body. All the above results suggest that the $NaGdF_4$ nanoparticles are rather safer at the current dose level in mice.

In the clinical trials, there is growing concern regarding the adverse side effects of Gd-based contrast agents on patients with damaged renal function (*13*). To address this concern, the biosafety of $NaGdF_4$ nanoparticles was assessed on renal failure rats. The experimental scheme is following with procedures in the previous work (*13*). Specifically, adenine-induced chronic renal failure (CRF) rat models were established through gastric gavage of adenine for 28 days. After the establishment of the rat models, 15 CRF rats were randomly divided into three groups ($n = 5$). Among them, two groups were intravenously injected with $NaGdF_4$ nanoparticles or Gd-DTPA with the dosage of 0.1 mmol Gd per kg weight, respectively, and the final group was served as the control and received no injections. Apart from CRF rats, 10 healthy rats were also adopted and randomly divided into two groups, in which one group of mice were treated with $NaGdF_4$ (0.1 mmol/kg), and the other group of mice was set as the control without administration.

The body weight variations of the different groups of rats were recorded every 2 days. As indicated in Fig. 8A, although the average body weight of CRF rats was lower than that of healthy rats, the injection of $NaGdF_4$ nanoparticles did not affect the trend of weight increase in either healthy rats or CRF rats. These results suggested that $NaGdF_4$ would not lead to the deterioration of the renal disease. During the 28 days, the blood tests were conducted every week to investigate the impact of $NaGdF_4$ nanoparticles on the hepatic and renal function of rats. As a result, the renal function related–blood markers such as CREA and UREA were significantly up-regulated compared with healthy rats (Fig. 8B). However, there were no obvious differences observed among the $NaGdF_4$-injected CRF rats, Gd-DTPA–injected CRF rats, and the non-injected CRF rats. In addition, there were no significant variations in the levels of serum P and Ca among five different groups of rats. These results indicated that although the $NaGdF_4$ did not alleviate the renal injury in the CRF rats, and it did not lead to the significant differences in renal-related blood indexes compared to the non-injected healthy/CRF rats. In addition, the hepatic function indicators including total bilirubin (TBIL), direct bilirubin (DBIL), indirect bilirubin (IBIL), and ALT were also measured. As indicated in Fig. 8C, there were no significant difference observed in these indexes among the five groups of rats, suggesting that the $NaGdF_4$ or Gd-DTPA injection did not affect the basic hepatic function of either CRF or healthy rats.

In addition to further confirm the biosafety of the $NaGdF_4$ nanoparticles, the rats were euthanized at 28 days after administration, and their kidneys and livers were extracted for histological analysis. As shown in Fig. 8D, the kidneys of healthy rats exhibited reddish-brown color with a lustrous appearance and smooth surfaces without swelling. In contrast, the kidneys extracted from CRF rats were visibly swollen and exhibited an abnormal pale color with dark spots. There was no notable difference observed between the kidneys of rats injected with nanoparticles and those that were not injected. To evaluate the pathological variation of kidneys among these groups, the kidney tissues were cut into slices and subjected to H&E staining (Fig. 8F). The results revealed that the kidney slices from healthy rat and $NaGdF_4$-injected healthy rat displayed normal morphological structures without obvious pathological changes. In comparison, the kidney tissues from CRF rats exhibited obvious degenerative variations, such as interstitial fibrosis, glomerulosclerosis and atrophy, tubular necrosis, and swelling of tubular epithelial cells. In addition to the H&E staining, the Masson staining was also used to evaluate the degree of renal fibrosis. As shown in fig. S12, the kidneys of the representative CRF rat exhibited severe renal fibrosis, as evidenced by the presence of intense blue signals. Nevertheless,

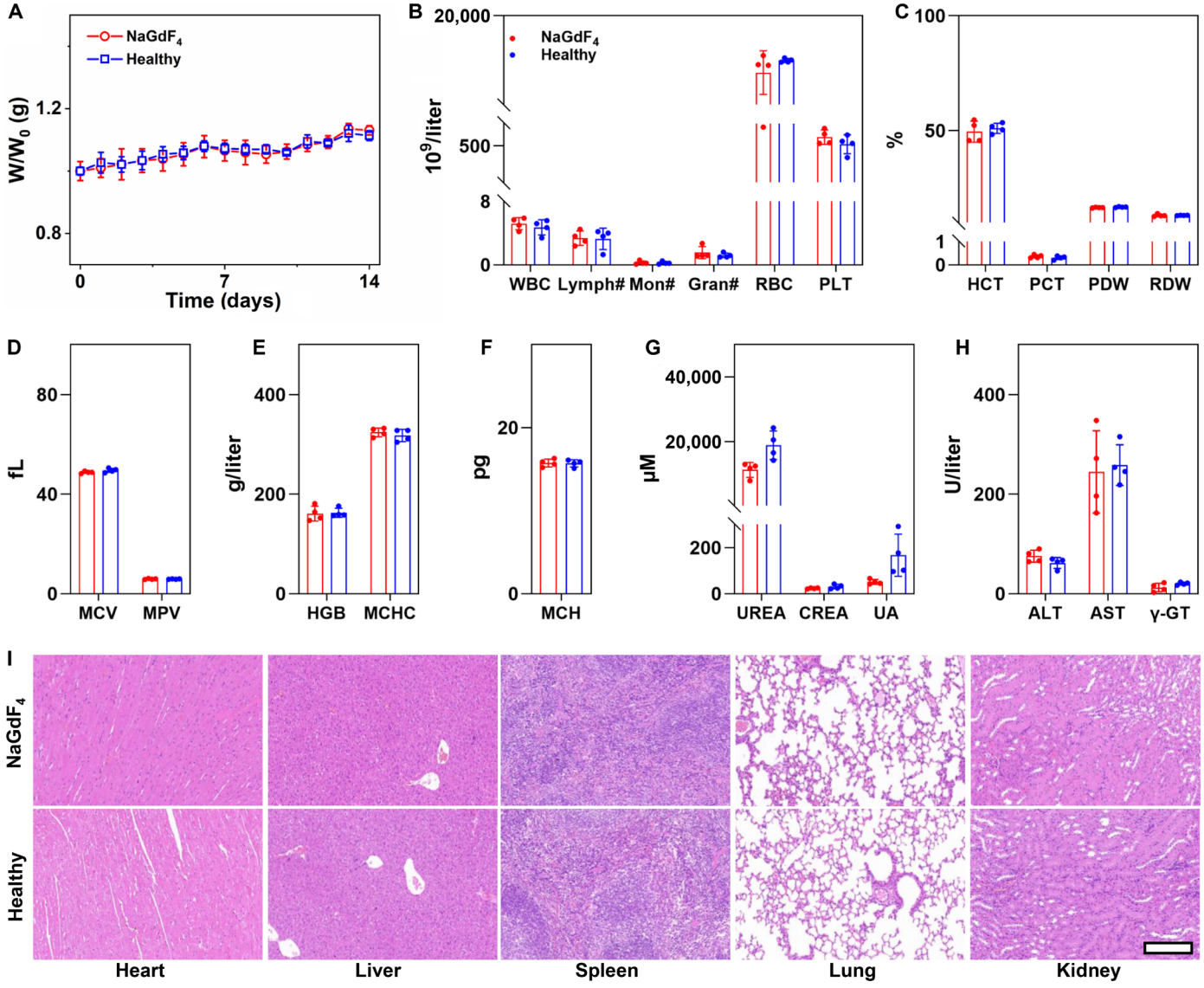

Fig. 7. Biosafety evaluation of $NaGdF_4$ on mice. (**A**) Fluctuations in the body weight of mice after $NaGdF_4$ nanoparticles administration ($n = 4$). (**B** to **H**) Blood biochemical test and routine blood test results of mice treated with the $NaGdF_4$ nanoparticles ($n = 4$). (**I**) H&E staining of the tissue slices from major organs of mice receiving $NaGdF_4$ and healthy mice. Data were plotted as means ± SD. The embedded scale bar corresponded to 200 μm. Abbreviations: ALT, alanine aminotransferase; AST, aspartate aminotransferase; WBC, white blood cell; Lymph#, lymphocytes; Mon#, monocyte ratio; Gran#, granulocyte; RBC, red blood cell; PLT, platelets; PDW, platelet distribution width; RDW, red cell distribution width; HGB, hemoglobin; MCHC, mean corpuscular hemoglobin concentration; HCT, hematocrit; PCT, plateletcrit; MCV, mean corpuscular volume; MPV, mean platelet volume; MCH, mean corpuscular hemoglobin; UREA, carbamide; CREA, creatinine; UA, uric acid; γ-GT, gamma-glutamyltransferase.

there was no obvious difference observed in morphological characteristics and fibrosis degrees between the kidney tissues from the nanoparticle-injected healthy/CRF rats and non-injected healthy/CRF rats, confirming the safety of $NaGdF_4$ nanoparticles in the patients with renal dysfunctions. In addition to kidneys, the livers of CRF rats and healthy rats were extracted for further biosafety evaluation as well. As displayed in Fig. 8E, there was no notable distinction in appearance among these extracted liver tissues. In addition, neither abnormal morphological variations nor fibrosis could be observed in the liver slices from these different groups, as evidenced by H&E (Fig. 8G) and Masson staining (fig. S13). These results indicated that the nanoparticles injection would not lead to the liver injury at this dosage. In recent years, clinical case reports have indicated that the exposure of Gd-based contrast agents to patients with renal impairment may lead to the development nephrogenic systemic fibrosis (NSF), a condition marked by fibrosis of the connective tissue in the skin and systemic tissues. To inspect this scena, the skin, heart, spleen, and lung tissues of rats were obtained for histological analysis. On the basis of the H&E staining shown in figs. S14 and S15, there were no morphological abnormalities in any of these tissues, providing evidence that the risk of developing NSF due to $NaGdF_4$ is not higher than that associated with Gd-DTPA. All the above results notably indicated that the $NaGdF_4$ nanoparticles would not cause the adverse side effect in both healthy animals and

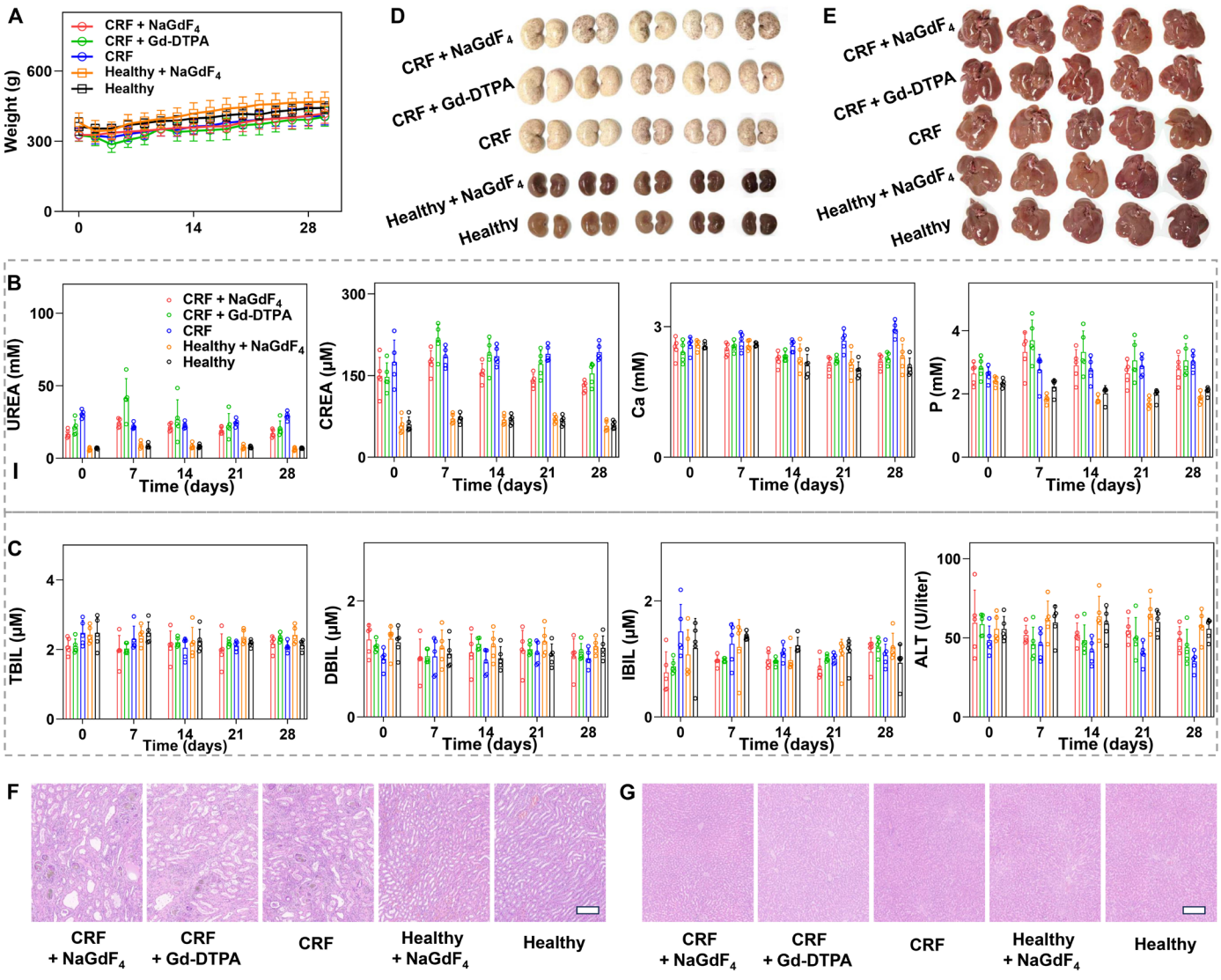

Fig. 8. Biosafety evaluation of $NaGdF_4$ on CRF rats. (**A**) Fluctuations in the body weight of mice after $NaGdF_4$ nanoparticles administration ($n = 5$). (**B** and **C**) Blood test results of different groups of rats ($n = 5$). Data were plotted as means ± SD. (**D**) Photographs of the extracted kidney tissues from healthy rats or CRF rats receiving different contrast agents. (**E**) Photographs of the extracted liver tissues from healthy rats or CRF rats receiving different contrast agents. The H&E staining images of kidney (**F**) and liver (**G**). The embedded scale bar corresponded to 200 μm. Abbreviations: UREA, carbamide; CREA, creatinine; Ca, calcium; P, phosphorus; TBIL, total bilirubin; DBIL, direct bilirubin; IBIL, indirect bilirubin; ALT, alanine aminotransferase.

animals with renal dysfunctions, further extremely confirming the biosafety of $NaGdF_4$ nanoparticles and highlighting their promising potential for clinical application.

Biosafety assessment of $NaGdF_4$ on large animals

In addition to the biosafety evaluation on rodent animals, the biosafety of $NaGdF_4$ was further assessed on young swine. The behavior of the young swine was monitored and recorded daily for 2 weeks after imaging experiments. As a result, no abnormalities in eating, drinking, urination, or neurological status were observed during the experimental period. As shown in fig. S16, after injection of $NaGdF_4$ nanoparticles, the body weight of the young swine continued to increase within 14 days from 7.2 to 9.6 kg, and the rectal temperature of swine remained stable without any abnormal fluctuations.

Furthermore, the blood routine and chemical tests were performed on the swine before and at 14 days after the injection of the $NaGdF_4$ nanoparticles to assess the side effects (figs. S17 and S18). The blood results showed no obvious increase or decrease at 14 days after injection, following all the parameters in the normal range. In detail, the liver function markers (ALT, AST, TBIL, DBIL, and IBIL) and kidney function markers (CREA, UA, etc.) were at a normal level. In addition, $NaGdF_4$ nanoparticles would not induce the inflammation-related disease or acute hemolysis verified by the results of WBC, Lymph#, RBC, PLT, MPV, and PCT.

To assess the potential tissue injury after intravenous injection of $NaGdF_4$ nanoparticles, the swine was euthanized at 14 days after the injection of nanoparticles; the main organs including the brain, heart, liver, spleen, lung, kidney, and bladder were acquired; and the

corresponding slices were stained with H&E. It was obvious in fig. S19 that there were no abnormal changes in the pathological histology or cellular structure, suggesting that $NaGdF_4$ nanoparticles did not induce any inflammation or damage to major organs. To confirm the elimination of $NaGdF_4$ from the body after 14 days after injection, CPN III rare-earth staining was conducted. As illustrated in fig. S20, no blue or cyan color can be observed in the slices of these organs after 14 days after injection, suggesting that most $NaGdF_4$ have been eliminated from the body. All the above results reveal that the $NaGdF_4$ nanoparticles have high biosecurity on large animals, establishing a strong foundation for the clinical translation.

DISCUSSION

Multiparametric MRI plays a crucial role in obtaining complementary information from different imaging sequences. By combining the advantages of different imaging sequences, it effectively reduces information uncertainty and enhances the accuracy of clinical diagnosis and segmentation. In previous publications, many attempts have been made to design and prepare dual-modality MRI agents that have both T_1 and T_2 contrast enhancement capabilities. For example, certain magnetic materials, such as ultrasmall iron oxide nanoparticles, exhibit contrast enhancement effects for both T_1 and T_2 imaging owing to their intrinsic properties, which have the potential to serve as T_1/T_2 dual-modality contrast agents. However, achieving precise control over the synthesis of iron oxide nanoparticles with a suitable diameter for use as T_1/T_2 dual-modality MRI contrast agents presents a dilemma. Larger size iron oxide nanoparticles exhibited high r_2 value, which impedes their use as T_1 contrast agents. In contrast, smaller size iron oxide nanoparticles have the potential to be used as T_1 contrast agents, but their T_2 effect is limited because of their smaller magnetic moment. Consequently, finding a balance between enhancing T_1 and T_2 contrast effects remains a challenging task. Another alternative strategy for achieving T_1/ T_2 dual-modality contrast agents is to integrate T_1 and T_2 components through covalent or noncovalent conjugation routes. For example, Park *et al.* conjugated Gd chelates onto Fe_3O_4 nanoparticles to obtain dual-modality T_1- and T_2-weighted MR contrast agent (*21*, *40*). Cheon *et al.* prepared core/shell/shell nanoparticles as T_1-T_2 dual-modality contrast agents by using a superparamagnetic nanoparticle as the core, SiO_2 as a separating layer, and a paramagnetic material as the outer shell (*41*, *42*). Although these dual-modality contrast agents can exhibit both T_1 and T_2 enhanced effect, the relaxation process of paramagnetic T_1 components can be easily disturbed by the magnetic field generated by superparamagnetic T_2 components. In particular, when these two components are in close proximity, the spin fluctuation of the T_1 component slows down and no longer facilitates water proton relaxation, resulting in the suppression of the T_1 enhancement effect. Therefore, this strategy may not be satisfactory for constructing a T_1/T_2 dual-modality contrast agent due to the intrinsic interference between T_1 and T_2 components.

The current studies can address the dilemma of the multiparametric MRI. The ultrasmall sized $NaGdF_4$ nanoparticles have strong T_1 and DCE effect because of their large surface area with seven unpaired electrons. With longer τ_R. The r_1 of nanoparticles was much larger than that of clinically used T_1 contrast agent, i.e., Gd chelates. The intrinsic magnetism and magnetic anisotropy of the $NaGdF_4$ crystal will largely amplify the magnetic susceptibility of free Gd ions. This property allows the nanoparticles to disrupt the uniformity of the local magnetic field, resulting in a loss of phase coherence in neighboring protons. Consequently, the nanoparticles can also serve as T_2 star and SWI contrast agent. Thus, the current design effectively bypasses the contradiction between T_1 and T_2 contrast enhancement, realizing the multiparametric MRI.

Upon the nanoparticle-based multiparametric MRI strategy proposed in the current study, the complementary vascular information can be acquired by combining the advantages of different imaging sequences. Specifically, through the utilization of enhanced 3D MRA, a quickly delineation of the anatomical structure of vascular systems in the region of interest is possible. The spatial distribution information, including every branch of large arteries and veins, as well as any abnormal morphological variations of the vasculatures, can be directly visualized. Different from angiography, T_1WI allows for mapping of not only the vasculatures but also the surrounding tissues with higher resolution. Therefore, the correlations between the vessels and tissues can be better understood through enhanced T_1-weighted images. As for the enhanced SWI, with the characteristics that are highly sensitive to the magnetic susceptibility difference, the microvessels, which exhibit negative signals, can be delineated following nanoparticles administration. As indicated in the current studies, this imaging sequence is particularly suitable for cerebrovascular imaging. Undoubtedly, these MRI modalities offer a more extensive array of physiological and pathological information for specific clinical indications, thereby optimizing the effectiveness of the diagnostic process.

Apart from the imaging performance, the biosafety features of nanoparticles are a major concern that must be addressed. In the current studies, the biosafety features of $NaGdF_4$ nanoparticles have been systematically confirmed in healthy rodent animals, rodent animals with renal dysfunction, and healthy swine, with no adverse side effect observed. In the clinical practice, free Gd ions, leached from Gd-based contrast agents, are known to be very toxic. The U.S. Food and Drug Administration has issued a warning regarding the association regarding gadolinium-based MR contrast agents and NSF, which is a severe syndrome known to be caused by the body retention of free Gd ions. As compared to clinically used Gd chelates, which may release the free Gd^{3+} ion into the body during the metabolism process, the stability of $NaGdF_4$ nanoparticles is notably higher. In these nanoparticles, the Gd^{3+} ions are trapped within the lattice of the crystal structure, making it difficult for them to be released. This characteristic ensures the biosafety of the nanoparticles.

As is commonly understood, for the nanomaterials designed for in vivo applications, one major challenge is the large-scale production with high reproducibility. To address this issue, our previous publication has developed a robust flow synthesis approach for the large-scaled preparation of monodispersed rare-earth nanocrystals with controlled size and characteristics (*43*). This method can be carried out in a continuous and automated manner, which can avoid the man-made intervention, thereby notably enhancing the reproducibility of nanoparticles. This synthesis approach holds the promise of facilitating the large-scale production of nanoparticles, thereby meeting the anticipated requirements for clinical translation in the future.

Overall, this work established a universal approach for achieving MRI multimodal vascular imaging using PEGylated ultrasmall $NaGdF_4$ nanoparticles as a multiparametric MRI contrast agent.

The large-scaled preparation, high biosafety, and outstanding multimodalities MRI performance endow $NaGdF_4$ with great clinical translation prospect. It thus can be reasonably believed that $NaGdF_4$ is able to be competent for the diagnosis of multiple vascular diseases in large animals as well, just like in rodent models. With the biocompatible nature and satisfactory angiography performance, $NaGdF_4$ could be a potential candidate as the next-generation MRA contrast agent to assist comprehensive morphological evaluations of a variety of complicated blood vessels and vascular diseases, not limited to the vessels displayed in the current study.

MATERIALS AND METHODS

Experimental design

These studies were designed to evaluate the enhancement of ultrasmall $NaGdF_4$ nanoparticles on the contrast of multiparameter MRA, as well as the pharmacokinetics, biosafety features, and translational prospect of the $NaGdF_4$ nanoparticles. In vivo studies were generally preferred to assess the performance of nanoparticles, and animals were randomly assigned to different experimental groups at the onset of each study. Healthy mice, rats, and swine, together with the different disease models were adopted to evaluate the properties of $NaGdF_4$ nanoparticles in distinct aspects. In the biosafety evaluation experiments, researchers who performed data collection and analysis were blinded to group allocation and detailed materials information, and in MRI studies, researchers who performed data collection, analysis, and vascular identification were blinded to group allocation and detailed animals' information. In vitro studies and in vivo studies were performed with three replicates, unless otherwise noted. No data were excluded from the experiments.

Synthesis of oleate-capped $NaGdF_4$ nanoparticles

The $NaGdF_4$ nanoparticles were synthesized through the coprecipitation reaction at high temperature. First, 1 mmol $GdCl_3{\cdot}6H_2O$, 4 ml of OA, and 15 ml of ODE were mixed together in a 100-ml flask to obtain a mixture. Then, under a vacuum, the mixture was heated to 150°C and reacted for 30 min to form a homogeneous solution. Second, 2.5 mmol NaOH and 4 mmol NH_4F were dissolved in 10 ml of methanol solution to get the mixture, and the mixture was added dropwise in the cooled solution (50°C) of the step one. Then, the reaction system was stirred at 50°C overnight. Third, under a vacuum, the methanol was removed below 100°C, and then, under a gentle flow of nitrogen protection, the reaction system was heated to 270°C with the rate of 20°C/min. Last, the reaction was held for 40 min at 270°C and was cooled to room temperature to obtain the oleate-capped nanoparticles. The resultant nanoparticles were precipitated by ethanol, collected by centrifugation for several times and then redispersed in cyclohexane for further use.

Synthesis of PEGylated $NaGdF_4$ nanoparticles

Ten milligrams of oleate-capped $NaGdF_4$ nanoparticles and 100 mg of asymmetric PEG were dissolved in 10 ml of tetrahydrofuran in a flask, and the mixture was magnetic stirred at 40°C. Then, the resultant PEGylated nanoparticles were precipitated by cyclohexane, collected by centrifugation for several times, and finally dried under vacuum at room temperature. The obtained nanoparticles were further purified through ultrafiltration with 30 kDa MWCO centrifugal filter (Millipore, YM-50) for four cycles at 2000*g* to remove the free ligand, and then dispersed in Milli-Q water for further use.

Relaxivity measurements

The Relaxivity measurements were performed on a 1.5-T clinical MRI instrument (iSpace Pro 1.5 T, Beijing Wandong Medical Technology Co. Ltd., Beijing, China). Briefly, a series of aqueous solutions of the PEGylated $NaGdF_4$ nanoparticles were prepared in 2.0-ml Eppendorf tubes. The parameters for T_1WI were set as follows: echo time (TE) = 12.58 ms; repetition time (TR) = 400 ms; NEX = 6; Echo train length (ETL) = 10; Matrix (MTX) = 360 × 360. The detailed parameters for T_2WI were set as follows: TE = 28 ms; TR = 1000 ms; NEX = 6; ETL = 10; MTX = 360 × 360. The parameters for T_1 value were measurement by 2D-Fast Gradient Recalled Echo sequence. The detailed parameters: TE = 8 ms; TR = 300, 500, 700, 900, 1100, 1300, 1500 ms; NEX = 1; ETL = 1; MTX = 128 × 128. T_2 value was obtained through 2D-Fast Gradient Recalled Echo sequence. The detailed parameters: TE = 8, 12, 16, 20, 24, 28 ms; TR =1000 ms; NEX = 1, ETL = 1; MTX = 128 × 128.

Animal studies

Animal studies are involved the rodent animals and large animals. The rodent animals in the studies involved BALB/c mice, C57BL/6J mice, and Sprague-Dawley rats. All the healthy mice (no genetic modification) including 6- to 8-week-old female BALB/c mice, 7-month-old male wild-type C57BL/6J mice, and male Sprague-Dawley rats of the desired age were purchased from SiPeiFu Biotechnology Co. Ltd. The 7-month-old male APP/PS1 transgenic AD mice were provided by Beijing HFK Bioscience Co. Ltd. Mice and rats were cohoused respectively and maintained on a 12-hour light-dark cycle with free access to food and autoclaved water in an air-conditioned specific pathogen–free level animal room (22° ± 1°C, 50 to 60% humidity, four mice per cage, two rats per cage). The 2-month male healthy bama swines were purchased from Sichuan Greentech Bioscience Co. Ltd.

In vivo imaging of animals

The following procedures are the methods of in vivo imaging of animals described in the previous work (*13*).

In vivo MRI of rodent animals

All in vivo MRI scannings of rodent animal models were performed on a 7-T animal MRI instrument (Bruker BioSpec, 70/20). During scanning, all the rodent animals were anesthetized with 1% isoflurane delivered via a nose cone, and the 0.1 mmol/kg PEGylated $NaGdF_4$ nanoparticles were intravenously injected through the tail vein. The different MRI sequences including 3D DCE angiography, T_1WI, SWI, and TOF angiography at different time point were selectively acquired through corresponding coil according to the demand.

In vivo PET imaging of rodent animals

All PET images were obtained by using an Inveon small animal PET scanner (Siemens Medical Solutions USA Inc.) at 1, 2, and 3 hours after injection. Before imaging, the 6-week-old female BALB/c mice (n = 3) were injected intravenously with 11.1 to 13 MBq of [^{68}Ga] PEGylated $NaGdF_4$ nanoparticles. During imaging, all mice were anesthetized with 2% isoflurane delivered via a nose cone and placed in the scanner in a prone position. Last, the PET images were reconstructed using a 3D-ordered subset expectation maximization algorithm.

In vivo MRI of swine

MRI of swine was performed following our previous procedures (*13*) on a 3-T human MRI instrument (GE SIGNA PET/MR). After being anesthetized with Zoletil 50 delivered via intramuscular

injection (3 mg/kg for the first time and 3 mg/kg for maintaining anesthesia), the swine were subjected to the imaging equipment, and the $NaGdF_4$ (0.1 mmol Gd/kg body weight) or Gd-DTPA (0.1 mmol Gd/kg body weight) were intravenously injected into the swine through small saphenous vein of hind leg. The human head coil was adopted for imaging. The different MRI sequences including 3D-TRICKS, 3D BRAVO, and SWAN at designed time points pre- and post-injection. All animal experiments were performed according to a protocol approved by the China-Japan Friendship Hospital Institutional Animal Care and Use Committee (zryhyy61-21-03-27).

Statistical analysis

Data are expressed as means ± SD as indicated in the figure captions. Statistical differences of two groups were determined by *T* test. A *P* value of <0.05 was regarded as statistically different. All tests were carried out by GraphPad Prism software (v7.0 and v8.0), and the charts were drawn by OriginPro (9.0 and 2019b) and GraphPad Prism software (v8.0).

Supplementary Materials

The PDF file includes:

Supplementary Text
Supplementary Materials and Methods
Figs. S1 to S20
Legends for movies S1 to S9

Other Supplementary Material for this manuscript includes the following:

Movies S1 to S9

REFERENCES AND NOTES

1. X. Suowen, I. Iqra, J. L. Peter, L. Hong, K. Danielle, Z. Xueying, L. Sihui, L. Zhuoming, L. Peiqing, H. Jihong, C. H. Ian, E. E. Eno, J. C. Scott, G. S. Alastair, W. Jianping, Endothelial dysfunction in atherosclerotic cardiovascular diseases and beyond: From mechanism to pharmacotherapies. *Pharmacol. Rev.* **73**, 924–967 (2021).
2. Y. Hu, Y. Zhao, P. Li, H. Lu, H. Li, J. Ge, Hypoxia and panvascular diseases: Exploring the role of hypoxia-inducible factors in vascular smooth muscle cells under panvascular pathologies. *Sci. Bull.* **68**, 1954–1974 (2023).
3. P. Musialek, L. Montauk, A. Saugnet, A. Micari, L. N. Hopkins, The cardio-vascular future of panvascular medicine: The basics. *Kardiol. Pol.* **77**, 899–901 (2019).
4. D. F. Guthaner, L. Wexler, D. R. Enzmann, S. J. Riederer, G. S. Keyes, W. F. Collins, W. R. Brody, Evaluation of peripheral vascular disease using digital subtraction angiography. *Radiology* **147**, 393–398 (1983).
5. A. Singh, V. Mor-Avi, A. R. Patel, The role of computed tomography myocardial perfusion imaging in clinical practice. *J. Cardiovasc. Comput.* **14**, 185–194 (2020).
6. A. Sabarudin, C. Subramaniam, Z. Sun, Cerebral CT angiography and CT perfusion in acute stroke detection: A systematic review of diagnostic value. *Imaging Med. Surg.* **4**, 282–290 (2014).
7. P. Zhang, Y. Feng, L. Zhu, K. Xu, Q. Ouyang, J. Zeng, F. Qin, N. Zhang, Y. Wang, F. He, Y. Shi, G. Chen, Z. Shi, M. Qin, Y. Hou, M. Gao, Predicting thrombolytic haemorrhage risk of acute ischemic stroke through angiogenesis/inflammation dual-targeted MR imaging. *Nano Today* **48**, 101707 (2023).
8. P. Vilela, H. A. Rowley, Brain ischemia: CT and MRI techniques in acute ischemic stroke. *Eur. J. Radiol.* **96**, 162–172 (2017).
9. E. J. Duffis, P. Jethwa, G. Gupta, K. Bonello, C. D. Gandhi, C. J. Prestigiacomo, Accuracy of computed tomographic angiography compared to digital subtraction angiography in the diagnosis of intracranial stenosis and its impact on clinical decision-making. *J. Stroke Cerebrovasc.* **22**, 1013–1017 (2013).
10. J. Chen, J. Einstein Andrew, R. Fazel, M. Krumholz Harlan, Y. Wang, S. Ross Joseph, H. Ting Henry, D. Shah Nilay, K. Nasir, K. Nallamothu Brahmajee, Cumulative exposure to ionizing radiation from diagnostic and therapeutic cardiac imaging procedures. *J. Am. Coll. Cardiol.* **56**, 702–711 (2010).
11. M. Cohnen, H. J. Wittsack, S. Assadi, K. Muskalla, A. Ringelstein, L. W. Poll, A. Saleh, U. Mödder, Radiation exposure of patients in comprehensive computed tomography of the head in acute stroke. *Am. J. Neuroradiol.* **27**, 1741–1745 (2006).
12. F. M. Amin, M. S. Asghar, A. Hougaard, A. E. Hansen, V. A. Larsen, P. J. H. de Koning, H. B. W. Larsson, J. Olesen, M. Ashina, Magnetic resonance angiography of intracranial and extracranial arteries in patients with spontaneous migraine without aura: A cross-sectional study. *Lancet Neurol.* **12**, 454–461 (2013).
13. P. Zhang, J. Cheng, Y. Lu, N. Zhang, X. Wu, H. Lin, W. Li, J. Wang, M. A. Winnik, Z. Gan, Y. Hou, Hypersensitive MR angiography based on interlocking stratagem for diagnosis of cardiac-cerebral vascular diseases. *Nat. Commun.* **14**, 6149 (2023).
14. S. Potthast, J. H. Maki, Non–contrast-enhanced MR imaging of the renal arteries. *Magn. Reson. Imaging Clin. N. Am.* **16**, 573–584 (2008).
15. A. J. Wheaton, M. Miyazaki, Non-contrast enhanced MR angiography: Physical principles. *J. Magn. Reson. Imaging* **36**, 286–304 (2012).
16. J. Estelrich, M. J. Sánchez-Martín, M. A. Busquets, Nanoparticles in magnetic resonance imaging: From simple to dual contrast agents. *Int. J. Nanomedicine* **10**, 1727–1741 (2015).
17. Y. Hou, R. Qiao, F. Fang, X. Wang, M. Gao, $NaGdF_4$ nanoparticle-based molecular probes for magnetic resonance imaging of intraperitoneal tumor xenografts in vivo. *ACS Nano* **7**, 330–338 (2013).
18. T. Martín-Noguerol, L. Concepción-Aramendia, C. C. T. Lim, E. Santos-Armentia, A. Cabrera-Zubizarreta, A. Luna, Conventional and advanced MRI evaluation of brain vascular malformations. *J. Neuroimaging* **31**, 428–445 (2021).
19. P. Zhang, W. Li, C. Liu, L. Zhu, J. Cheng, R. Pang, Y. Lan, M. Qin, Y. Hou, Simultaneous identifying the infarct core, collaterals, and penumbra after acute ischemic stroke with a low-immunogenic MRI nanoprobe. *Mater. Design* **233**, 112211 (2023).
20. P. Zhang, W. Li, C. Liu, F. Qin, Y. Lu, M. Qin, Y. Hou, Molecular imaging of tumour-associated pathological biomarkers with smart nanoprobe: From "seeing" to "measuring". *Exp. Dermatol.* **3**, 20230070 (2023).
21. H. Yang, Y. Zhuang, Y. Sun, A. Dai, X. Shi, D. Wu, F. Li, H. Hu, S. Yang, Targeted dual-contrast T1- and T2-weighted magnetic resonance imaging of tumors using multifunctional gadolinium-labeled superparamagnetic iron oxide nanoparticles. *Biomaterials* **32**, 4584–4593 (2011).
22. L. Wang, J. Huang, H. Chen, H. Wu, Y. Xu, Y. Li, H. Yi, Y. A. Wang, L. Yang, H. Mao, Exerting enhanced permeability and retention effect driven delivery by ultrafine iron oxide nanoparticles with T_1–T_2 switchable magnetic resonance imaging contrast. *ACS Nano* **11**, 4582–4592 (2017).
23. P. Zhang, J. Zeng, Y. Li, C. Yang, J. Meng, Y. Hou, M. Gao, Quantitative mapping of glutathione within intracranial tumors through interlocked MRI signals of a responsive nanoprobe. *Angew. Chem. Int. Engl.* **60**, 8130–8138 (2021).
24. G. Fananapazir, D. Marin, P. V. Suhocki, C. Y. Kim, M. R. Bashir, Vascular artifact mimicking thrombosis on MR imaging using ferumoxytol as a contrast agent in abdominal vascular assessment. *J. Vas. Interv. Radiol.* **25**, 969–976 (2014).
25. N. J. J. Johnson, W. Oakden, G. J. Stanisz, R. Scott Prosser, F. C. J. M. van Veggel, Size-tunable ultrasmall $NaGdF_4$ nanoparticles: Insights into their T_1 MRI contrast enhancement. *Chem. Mater.* **23**, 3714–3722 (2011).
26. K.-H. Diehl, R. Hull, D. Morton, R. Pfister, Y. Rabemampianina, D. Smith, J.-M. Vidal, C. V. D. Vorstenbosch, A good practice guide to the administration of substances and removal of blood, including routes and volumes. *J. Appl. Toxicol.* **21**, 15–23 (2001).
27. E. P. Rondon, H. A. Benabdoun, F. Vallières, M. Segalla Petrônio, M. J. Tiera, M. Benderdour, J. C. Fernandes, Evidence supporting the safety of pegylated diethylaminoethyl-chitosan polymer as a nanovector for gene therapy applications. *Int. J. Nanomedicine* **15**, 6183–6200 (2020).
28. Y. Yan, X. Sun, B. Shen, Contrast agents in dynamic contrast-enhanced magnetic resonance imaging. *Oncotarget* **8**, 43491–43505 (2017).
29. I. Ferrer, N. Vidal, Chapter 7 - Neuropathology of cerebrovascular diseases. *Handb. Clin. Neurol.* **145**, 79–114 (2017).
30. U. Lendahl, P. Nilsson, C. Betsholtz, Emerging links between cerebrovascular and neurodegenerative diseases—A special role for pericytes. *EMBO Rep.* **20**, e48070 (2019).
31. N. Korte, R. Nortley, D. Attwell, Cerebral blood flow decrease as an early pathological mechanism in Alzheimer's disease. *Acta Neuropathol.* **140**, 793–810 (2020).
32. T. Gargadennec, G. Ferraro, R. Chapusette, X. Chapalain, E. Bogossian, M. Van Wettere, L. Peluso, J. Creteur, O. Huet, N. Sadeghi, F. S. Taccone, Detection of cerebral hypoperfusion with a dynamic hyperoxia test using brain oxygenation pressure monitoring. *Crit. Care* **26**, 35 (2022).
33. C. I. Wu, S. P. Changlai, W. S. Huang, C. H. Tsai, C. C. Lee, C. H. Kao, Usefulness of 99mTc ethyl cysteinate dimer brain SPECT to detect abnormal regional cerebral blood flow in patients with acute carbon monoxide poisoning. *Nucl. Med. Commun.* **24**, 1185–1188 (2003).
34. I. Uwano, K. Kudo, M. Sasaki, S. Christensen, L. Østergaard, K. Ogasawara, A. Ogawa, CT and MR perfusion can discriminate severe cerebral hypoperfusion from perfusion absence: Evaluation of different commercial software packages by using digital phantoms. *Neuroradiology* **54**, 467–474 (2012).
35. D. Klakotskaia, C. Agca, R. A. Richardson, E. G. Stopa, T. R. Schachtman, Y. Agca, Memory deficiency, cerebral amyloid angiopathy, and amyloid-β plaques in APP+PS1 double transgenic rat model of Alzheimer's disease. *PLOS ONE* **13**, e0195469 (2018).

36. L. Wei, J. P. Erinjeri, C. M. Rovainen, T. A. Woolsey, Collateral growth and angiogenesis around cortical stroke. *Stroke* **32**, 2179–2184 (2001).
37. A. Mettouchi, The role of extracellular matrix in vascular branching morphogenesis. *Cell Adh. Migr.* **6**, 528–534 (2012).
38. C. Wang, Y. Yang, M. Xu, F. Mao, P. Yang, S. Yuan, R. Gao, S. Gan, Deep sequencing of the rat MCAO cortexes reveals crucial circRNAs involved in early stroke events and their regulatory networks. *Neural Plast.* **2021**, 9942537 (2021).
39. A. Kádár, G. Wittmann, Z. Liposits, C. Fekete, Improved method for combination of immunocytochemistry and Nissl staining. *J. Neurosci. Methods* **184**, 115–118 (2009).
40. K. H. Bae, Y. B. Kim, Y. Lee, J. Hwang, H. Park, T. G. Park, Bioinspired synthesis and characterization of gadolinium-labeled magnetite nanoparticles for dual contrast T_1- and T_2-weighted magnetic resonance imaging. *Bioconjug. Chem.* **21**, 505–512 (2010).
41. T.-H. Shin, J. Choi, S. Yun, I.-S. Kim, H.-T. Song, Y. Kim, K. I. Park, J. Cheon, T_1 and T_2 dual-mode MRI contrast agent for enhancing accuracy by engineered nanomaterials. *ACS Nano* **8**, 3393–3401 (2014).
42. J. Choi, J.-H. Lee, T.-H. Shin, H.-T. Song, E. Y. Kim, J. Cheon, Self-confirming "AND" logic nanoparticles for fault-free MRI. *J. Am. Chem. Soc.* **132**, 11015–11017 (2010).
43. M. Jiao, L. Jing, C. Liu, Y. Hou, J. Huang, X. Wei, M. Gao, Differently sized magnetic/upconversion luminescent $NaGdF_4$:Yb,Er nanocrystals: Flow synthesis and solvent effects. *Chem. Commun.* **52**, 5872–5875 (2016).

Acknowledgments: We thank Y. Feng, K. Xu, and W. Zhang from Beijing University of Chemical Technology for the help with respect to rodent model establishment. **Funding:** This work was supported by the National Natural Science Foundation of China (NSFC) (22177009), National Natural Science Foundation of China (NSFC) (52033001), National Natural Science Foundation of China (NSFC) (82102679), and Beijing Natural Science Foundation (7242138). **Author contributions:** Conceptualization: W.L., Z.G., P.Z., M.Q., and Y.H. Data curation: W.L., P.Z., and Y.H. Formal analysis: W.L., P.Z., and Y.H. Funding acquisition: P.Z., M.Q., and Y.H. Investigation: W.L., J.C., C.L., P.Z., and Y.H. Methodology: W.L., Z.G., P.Z., M.Q., and Y.H. Project administration: P.Z., M.Q., and Y.H. Resources: N.Z., H.L., F.H., and Y.H. Supervision: Z.G., P.Z., M.Q., and Y.H. Validation: W.L., P.Z., M.Q., and Y.H. Visualization: W.L., P.Z., and Y.H. Writing—original draft: W.L., P.Z., and Y.H. Writing—review and editing: W.L., J.C., C.L., N.Z., H.L., F.H., Z.G., P.Z., M.Q., and Y.H. **Competing interests:** The authors declare that they have no competing interests. **Data and materials availability:** All data needed to evaluate the conclusions in the paper are present in the paper and/or the Supplementary Materials.

Submitted 12 May 2024
Accepted 28 August 2024
Published 4 October 2024
10.1126/sciadv.adq4082